Biomaterials Advances 154 (2023) 213636

Contents lists available at ScienceDirect

Biomaterials Advances

journal homepage: www.journals.elsevier.com/materials-science-and-engineering-c

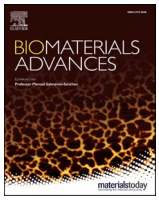

Fibroblasts mediate endothelium response to angiogenic cues in a newly developed 3D stroma engineered model

Alessandra Dellaquila [a,*], Chloé Dujardin [a], Chau Le Bao [a], Chloé Chaumeton [b], Albane Carré [a], Camille Le Guilcher [a], France Lam [b], Teresa Simon-Yarza [a,*]

[a] Université Paris Cité, Université Sorbonne Paris Nord, Laboratory for Vascular Translational Science, INSERM U1148, X. Bichat Hospital, Paris 75018, France
[b] Sorbonne Université, Institute of Biology Paris-Seine, Paris 75005, France

ARTICLE INFO

In memory of Dr. Susanne Bolte

Keywords:
Natural biopolymer
Vascular tissue engineering
3D stroma model
Multiscale characterization
In vitro drug testing
Lightsheet microscopy

ABSTRACT

Three-dimensional stroma engineered models would enable fundamental and applicative studies of human tissues interaction and remodeling in both physiological and pathological conditions. In this work, we propose a 3D vascularized stroma model to be used as *in vitro* platform for drug testing. A pullulan/dextran-based porous scaffold containing pre-patterned microchannels of 100 μm diameter is used for co-culturing of fibroblasts within the matrix pores and endothelial cells to form the lumen. Optical clearing of the constructs by hyperhydration allows for in-depth imaging of the model up to 1 mm by lightsheet and confocal microscopy. Our 3D vascularized stroma model allows for higher viability, metabolism and cytokines expression compared to a monocultured vascular model. Stroma-endothelium cross-talk is then investigated by exposing the system to pro and anti-angiogenic molecules. The results highlight the protective role played by fibroblasts on the vasculature, as demonstrated by decreased cytotoxicity, restoration of nitric oxide levels upon challenge, and sustained expression of endothelial markers CD31, vWF and VEGF. Our tissue model provides a 3D engineered platform for *in vitro* studies of stroma remodeling in angiogenesis-driven events, known to be a leading mechanism in diseased conditions, such as metastatic cancers, retinopathies and ischemia, and to investigate related potential therapies.

1. Introduction

Recent advances in manufacturing techniques and 3D cell culture methods have opened up the possibility to engineer human tissue models with remarkable physiological-like structure and behavior. The merger with other technologies, as microfluidics and organoids, has further widened the potential applications of tissue engineering (TE), which is nowadays not only limited to regenerative medicine in clinics but also used for *in vitro* modeling of pathophysiology, drug testing and therapy. [1] Nonetheless, the majority of the TE models proposed in literature still lack some fundamental features for a closer mimicry of the native organs, two of them being the vasculature and the tissue microenvironment. As the vascular network allows for gases and nutrients exchanges, its integration in artificial tissues is fundamental to mimic transport mechanisms and to ensure proper integration with the host tissue upon implantation. [2] Furthermore, the role of vascular tissue in participating to both physiological and pathological remodeling events is well known: angiogenesis, the process of forming new blood vessels from existing ones, is one of the main processes through which this remodeling occurs. [3] However, though largely studied, the role of many pro and anti-angiogenic factors and how they affect the cross-talk of a heterotypic culture model is often poorly understood. The use of *in vitro* models, such as organ-on-chips, has contributed in deciphering some of these mechanisms. However, these systems often suffer from major limitations, such as (i) fabrication with materials that are not biologically nor mechanically relevant, as silicon-based polymers, (ii) use of monocultures with endothelial cells, (iii) lack of 3D cellular spatial arrangement. [4–7]

Moreover, the stroma of human organs exerts a supporting and connective function for the parenchyma. Composed of fibroblasts, mesenchymal and hematopoietic cells, extracellular matrix, vasculature, nerves and lymphatic vessels, it is known to play a fundamental role during remodeling processes, as angiogenesis, wound healing and in pathologies involving fibrosis. [8] However, this tissue is underrepresented in TE and the majority of the existing models have focused on its function during tumor remodeling. [7,9–11] Artificial tissues that

* Corresponding authors.
E-mail addresses: alessandra.dellaquila@inserm.fr (A. Dellaquila), teresa.simon-yarza@inserm.fr (T. Simon-Yarza).

https://doi.org/10.1016/j.bioadv.2023.213636
Received 11 May 2023; Received in revised form 30 August 2023; Accepted 20 September 2023
Available online 22 September 2023

reproduce the stroma have been engineered, often in form of sheets or injectable gels, for cardiac repair and wound healing applications or as organ-on-chips for oncologic drug screening. [10,12–14] Porous scaffolds have been used to reproduce the stroma microenvironment for the study of pathological events, however these models were often limited to: (i) use of synthetic biomaterials, (ii) unmatching mechanical properties, (iii) lack of the endothelium. [15–17]

In this work, we propose a porous matrix made of pullulan and dextran, two natural biopolymers produced by fermentation by *Aureobasidium pullulan* fungus and *Leoconostoc mesenteroides* bacteria, respectively. Along with their biocompatibility and low immunogenicity, their physical properties can be easily tuned by modifying the manufacturing parameters. Thanks to their versatility, we have recently demonstrated their use in form of scaffolds or hydrogels for various applications, including study of endothelial behavior, 3D platform for neuronal growth and for the design of 3D liver microtissues. [18–22] Here, we developed a new formulation from these biomaterials in form of 3D porous scaffolds with inner microchannels to engineer a vascularized stroma model. Due to lack of cellular adhesion moieties of pullulan/dextran matrices, specific studies were conducted on the design of 3D collagen coating of inner structures (microchannels and/or pores) for selective adhesion of the different cell types. [22]

The manufacturing approach led to matrices with relevant physical properties and a co-culture setup enabled us to obtain a heterotypic platform, with distinct yet communicating fibroblast and endothelial cells (ECs) compartments.

The stroma co-culture model was investigated in comparison to a 3D vascular monoculture under physiological conditions and upon administration of either pro-angiogenic (hypoxia, addition of L-Arginine) or anti-angiogenic cues (bevacizumab, an anti-metastatic drug).

Development of a customized optical clearing method allowed for 3D volumetric imaging of the model while tissue response in terms of viability, metabolism, matrix remodeling, cytokines production and nitric oxide release was investigated by quantitative assays. Taken together, the results enlightened the protective role of fibroblasts on the vascular fraction and demonstrated the capability of this model to mimic physiological responses to external stimuli.

2. Materials and methods

2.1. Hydrogel solution preparation

The hydrogel PuD solution was composed of the polysaccharides pullulan (75 % *w*/w%, $M_w = 200$ kDa, Hayashibara, Japan) and dextran (25 % w/w%, $M_w = 500$ kDa, Pharmacosmos, Denmark), and sodium chloride (NaCl, $M_w = 58.44$, Fisher Chemical, USA) as porogen agent. The solution was prepared as previously described [23]: briefly, 9 g of pullulan powder, 3 g of dextran powder and 14 g of NaCl were weighted and mixed in distilled water (DI, 40 mL) by stirring (room temperature, RT, 1 h) to ensure proper homogenization. The solution was left for 24 h at RT for air bubbles removal.

2.2. Molding setup and 3D printing

Suture monofilaments were used as channel templates (polyropylene monofilament PROLENE™ 7/0 dec., ETHICON Inc., USA). A custom mold composed of pillars was designed in Fusion 360, AutoDesk to tie the filaments for molding and 3D printed (Ultimaker S3 printer, Cubeek3D, France) in polylactic acid (PLA): layer height of 0.2 mm, printing speed of 70 mm s^{-1} and printing temperature of 205 °C were set for PLA extrusion (Fig. S1b, Appendix). The molding setup was assembled as shown in Fig. S1a, Appendix: the suture filaments were wrapped around the pillars, and the PuD gel poured between two glass slides separated by 0.35–0.40 mm-thick spacers, sandwiching the filaments.

2.3. Scaffolds fabrication

PuD scaffolds were fabricated by molding/ cross-linking/ freeze-drying (FD) method. The hydrogels were prepared by following the protocol patented from our laboratory. [24] Briefly, sodium hydroxide (NaOH, 10 M, Sigma-Aldrich, USA) was added to 10 g of PuD solution for activation of the -OH chains and the mixture stirred (RT, 200 rpm, 15 min). In parallel, a solution of 3 % *w/v*% sodium trimetaphosphate (STMP, $Na_3O_9P_3$, Sigma-Aldrich) in DI water was prepared as chemical cross-linker. Addition of the STMP solution to the PuD was done in ice to slow down the cross-linking kinetics and the gel was then poured over the mold setup and placed in an oven (50 °C, 20 min) for complete cross-linking. Empty microchannels for the monoculture model were obtained by pulling out the suture filaments while in the vascularized stroma the filaments were kept in place to prevent stromal cells to access the channel. Then, cylindrical hydrogels were obtained by punching (5 mm in diameter). The hydrogels were placed in a 10X PBS bath under mechanical agitation for NaOH neutralization. After reaching neutral pH, consecutive rinsing steps in DI baths allowed for removal of the porogen agent (conductivity <10 μS cm^{-1}, conductivity meter 145 A+, Thermo Scientific Orion, USA). Porous PuD scaffolds were obtained by single freeze-drying (S-FD, Pilot −80 freeze dryer, Cryotec, France): the hydrogels were placed in a 0.025 % *w/v*% NaCl bath (final conductivity <500 μS cm^{-1}) and freeze-dried in polystyrene Petri dishes (Falcon, Corning, USA). A freezing speed of 0.5 °C min^{-1} was set until reaching −30 °C and maintained for 2.5 h. Primary freeze-drying was done with a vacuum of 0.05 mbar and with increasing temperature from −30 °C to 10 °C by imposing a step function and freeze-drying speeds of 0.1 °C min^{-1}. Finally, a fast secondary freeze-drying was performed at 0.001 mbar of pressure and 0.33 °C min^{-1} of speed until reaching RT. For PuD scaffolds freeze-dried twice, the matrices were re-hydrated in 0.025 % *w/v*% NaCl bath after the first freeze-drying for 2 h under shaking, then freeze-dried a second time (double freeze-drying, D-FD) with the same cycle as described above.

2.4. Collagen coating

PuD matrices were coated with collagen either before or after freeze-drying. Highly purified bovine corium acid solubilized collagen (FS22024, Collagen Solutions, UK) was diluted in 0.01 N HCl to obtain a final concentration of 1 mg mL^{-1}. The samples were placed in a sterile 15 mL syringe with the collagen solution (about 3 mL of solution were used to coat 15 gels). The collagen penetration within the PuD structure was obtained by vacuum impregnation, by flushing the solution back and forth. PuD gels were kept flat for at least 2 h at RT with no agitation to allow for collagen deposition. Then, the excess was removed by washing with PBS 1X for 5 min and with PBS 0.1X for 5 min under mild agitation to allow for collagen neutralization before the freeze-drying.

2.5. Scaffolds characterization

2.5.1. Physical properties

Porosity of freeze-dried scaffolds was evaluated by water squeezing method, as previously reported. [25] Briefly, porosity tests were carried out by soaking the specimens in PBS 1X for 2 h under mild mechanical shaking ($n \geq 3$ for each test, each formulation). The specimens were weighted (scale AG204 DeltaRange®, Mettler Toledo, USA) after removing the excess of liquid and after squeezing the liquid by gentle pressing with a spatula. The percentage porosity, representing the volume of macropores within the scaffold, was calculated as follows:

$$\text{Porosity}\ (\%) = 100 \bullet \left(M_i - M_f\right)/M_i \quad (1)$$

where M_i is the initial weight of the wet sample and M_f represents the final weight after squeezing. To investigate the matrix wettability, swelling measurements were conducted. Specimens were placed in oven

at 50 °C overnight to remove humidity, then they were soaked in PBS 1X and incubated at 37 °C to mimic cell culture conditions. At each time point (t = x), the sample was weighted after removing the excess of liquid ($M_s^{t=x}$). The swelling ratio was calculated as follows:

$$\text{Swelling Ratio} = \left(M_s^{t=x} - M_d\right)/M_d \quad (2)$$

where M_d indicates the initial weight of the specimen in dry state. The swelling ratio was determined for $t = 0$, 0.5, 1, 2, 6, 24, 48 and 72 h ($n \geq 3$ for each test, each formulation).

2.5.2. Mechanical properties: nanoindentation

The Young's modulus of coated and uncoated PuD scaffolds in wet state was studied by nanoindentation (PIUMA Nanoindenter, Optics11Life, Netherlands). Spherical probes with 0.45 N m^{-1} of stiffness and a tip radius of 103.5 μm or 0.49 N m^{-1} of stiffness and a tip radius of 109 μm were used. Samples were hydrated in PBS 1X at 37 °C until reaching the time-point of interest and consequently mounted. To ensure a flat positioning of the indented surface, 3 cm × 3 cm parafilm pieces were cut and punched to create a measurement window. The samples were placed in a plastic Petri dish and layered with the parafilm frame, after assuring the window was matching the sample surface. Nanoindentation measurements were performed in immersion in PBS at RT in nanoindentation control mode. Each specimen was analysed by a matrix scan of 3 × 3 points with displacements Δx and Δy of 25 μm). The Young's modulus was calculated using the Hertzian model, with 3000 nm of maximum indentation depth and a Poisson's ratio of 0.5. The data analysis was performed using the DataViewer V2.4 software.

2.5.3. Rheological measurements

The G′ and G″ of uncoated and coated PuD scaffolds after full hydration were investigated by rheometry (Elastosens, Rheolution, Canada). To ensure the contact with the sample holder's inner walls, hydrogels were cut after cross-linking with a 16G puncher and coated and freeze-dried as described above. Specimens were hydrated in PBS 1X at 37 °C for 48 h before the tests. The acquisition was performed over 5 min with a Δt of 20 s between each acquisition point. Specimens seeded with fibroblasts BJ were cultured for 7 days before performing the tests and the results compared to coated scaffolds without cells hydrated over 7 days in cell culture medium (FGM-2) and kept in incubator.

2.6. Collagen coating quantification

Samples coated by either single or double freeze-drying with collagen (1 mg mL^{-1}) were tested for determination of the collagen content by using a Pierce™ BCA Protein Assay Kit (23,225, Thermo Scientific), as per manufacturer instruction. Briefly, the specimens were incubated for 30 min at 37 °C with the working reagent and the supernatant absorbance was read at 562 nm with a microplate reader (Infinite® 200 PRO, Tecan, Switzerland). The collagen concentration for each scaffold formulation was calculated from the albumin standard (BSA) curve and compared to the data obtained for uncoated samples (negative control).

2.7. 2D and 3D Cell culture

Human vascular endothelial cells (ECs, HUV-EC-C, CRL-1730™, ATCC, USA) and human fibroblasts from neonatal normal foreskin (FBs, BJ CRL-2522™, ATCC) were cultured in standard tissue culture flasks in EGM™-2 (CC-3162, Lonza) and complete fibroblast medium (FGM™-2, CC-3132, Lonza, Switzerland), respectively. Scaffolds were prepared for cell culture by UV light sterilization for 2 h. After reaching 80 % confluency, cells were detached and diluted to the desired cell concentration: for the lumen formation, a final nominal concentration of 2 × 10^6 cells mL^{-1} was chosen, for the vascular stroma model, scaffolds were seeded with 2 × 10^6 cells mL^{-1} ECs and 3 × 10^6 cells mL^{-1} FBs and, for consistency of cellular density, the monocultured vascular model was seeded with 5 × 10^6 cells mL^{-1} ECs. For the coculture model, culture media were mixed with a ratio EGM™-2/ FGM™-2 of 1/1.5 % *v*/v%. The seeding of the scaffolds in dry state was performed by syringe-induced vacuum technique, as previously described by our group. [22] Briefly, the scaffolds and the cell culture suspension were placed into a 10 mL syringe barrel. A dual check valve was used to close the syringe after insertion of the plunger to apply a negative pressure. Then, a repetitive pushing – and - pulling force was applied to ensure proper scaffold hydration as well as cellular penetration within the matrix. To allow for homogeneous final cellular distribution, the seeding process was repeated twice (halved cell densities as indicated above for each seeding), with one-hour incubation between the two steps. Then, the seeded constructs were placed in cell culture media and incubated (37 °C, 5 % CO_2) and the medium changed every other day.

2.8. Response of mono and co-culture 3D models to external stimuli

Both monocultured vascular and vascularized stroma models were subjected to pro or anti-angiogenic chemical or physical cues to study the cellular response and the impact on the angiogenesis process. At Day 4 of culture under standard conditions, the scaffolds were exposed to each stimulus separately for 72 h. (i) In a first study, cell culture media were supplemented with 1 mM L-arginine (A8094, Merck, Germany), the main amino acid involved in nitric oxide (NO) production. (ii) In a second study, the scaffolds were subjected to hypoxic environment (1 % O_2, 5 % CO_2, 37 °C). (iii) In a third condition, the matrices were administered with 0.1 mg mL^{-1} bevacizumab 25 mg mL^{-1} (BEV, kind gift of Dr. J.-P. Desilles, Hôpital Fondation Adolphe de Rothschild, Paris, France), an anti-VEGF antibody. Analysis of the cellular viability, nitric oxide and angiogenesis-related proteins were performed after 24 h (d1) and 72 h (d3) administration. Samples were fixed at each time point and prepared for consecutive imaging.

2.9. Viability and metabolic activity studies

LDH and Live/Dead viability assays. The cell viability in the matrices was assessed by two distinct methods. First, a cytotoxicity assay, based on the measurement of lactate dehydrogenase (LDH) activity, was conducted (Cytotoxicity Detection Kit^{PLUS},744,934,001, Roche, Switzerland) according to the manufacturer's instructions. Positive controls (Ctrl +), corresponding to the maximal LDH release, were incubated in media supplemented with a lysis solution (10 % *v*/v%) for 15 min. Media only was used as blank while the samples were incubated in the reaction solution for 15 min. Readings were performed in absorbance at 490 nm and 690 nm with a microplate reader (Infinite® 200 PRO, Tecan). The cytotoxicity rate was determined from the absorbance readings as follows:

$$Cytotoxicity\ (\%) = 100\left(A_{Sample} - A_{Blank}\right)/\left(A_{Ctrl+} - A_{Blank}\right) \quad (3)$$

Secondly, Live/Dead staining was performed at Day 7. Calcein AM Viability Dye (65–0853-39, eBioscience™, Invitrogen™, USA) and ethidium homodimer (EthD-1, 46,043, Sigma-Aldrich) were diluted in media to a final concentration of 2 μM and 4 μM, respectively and living samples incubated in the staining solution for 1 h. After rinsing, imaging was performed by confocal microscopy (TCS SP8, Leica Microsystems, Germany).

2.10. Resazurin-based assay

The metabolic activity of seeded scaffolds was investigated by Resazurin- based assay (TOX8, 263–718-5, Sigma-Aldrich). Samples were incubated with Resazurin (10 % *v*/v% in warm cell culture media) for 3 h. Resazurin incubated in empty wells was used as negative control. Measures of the fluorescence intensity (560/590 nm exc/em) were

performed on the supernatant at Day 1, 3 and 7 from seeding with a microplate reader (Infinite® 200 PRO, Tecan).

2.11. Nitric oxide production studies

Quantification of NO was done by analysis of cell culture supernatant using a NO assay kit (ab272517, abcam, UK), as per manufacturer's instruction. Reading of the optical densities (Infinite® 200 PRO, Tecan) was done at 540 nm and NO fold change was calculated by normalization of absorbance values compared to the controls.

2.12. Cytokines expression studies

Analysis of angiogenesis markers was carried out by multiplex immunoassay of cell culture supernatants using customized detection kits, based on magnetic microparticles technology (Luminex® Discovery assay, LXSAHM, R&D Systems, USA): CD31/PECAM-1, bFGF, IL-8, VEGF and vWF-A2. An analogous kit was also used for the study of matrix metalloproteinases MMP-2 and MMP-9. The samples were prepared as per manufacturer's instruction and readings performed with a suspension array system (BioPlex – 200, Bio-Rad, USA). Data were analysed and averaged with the Bio-Plex Manager software (Bio-Rad).

2.13. Permeability assay - dynamic studies under perfusion

To investigate the lumen functionality, a permeability assay was performed by flowing FITC Dextran supplement medium and recording the fluorophore extravasation rate. A 30G needle (Agani, Terumo, Japan) was inserted into the scaffold microchannel and FITC Dextran 70 kDa (1 μM, Sigma-Aldrich) was perfused with a syringe pump (ExiGo Pulse-Free Microfluidic Syringe Pump, Cellix, Ireland) at a constant flow rate of 10 μL/min. The flow rate was chosen to mimic the wall shear stress typical of arterioles and venules (above 20 dyn cm^{-2}), according to the channel size (about 100 μm in diameter). Tests were conducted on unseeded scaffolds (hydrated for 7 days in PBS at 37 °C, negative control) and on living vascularized stroma constructs at d7 ($n = 3$ for each condition). The channel and the extravascular space were imaged every 3 min for 15 min (Axio Observer inverted microscope, Zeiss, Germany) and the images were analysed with Fiji, ImageJ by selecting 3 ROIs for the extravascular space and 2 ROIs along the channel. Permeability was calculated as previously reported: [6,27].

$$P = \left(I_{fe} - I_{ie}\right) \bullet \Delta x / \left(I_v - I_b\right) \bullet \Delta t \quad (4)$$

where P = permeability coefficient (μm s^{-1}), I_{fe} = final average fluorescence Intensity of the extravascular space, I_{ie} = initial average fluorescence Intensity of the extravascular space, I_v = total average fluorescence Intensity of the channel, I_b = background intensity at $t = 0$ min, Δt = difference in seconds between the final and initial time points and Δx = distance between the extravascular and channel ROIs.

2.14. Staining and immunolabeling

Fibroblasts and ECs were eventually pre stained with CellTracker™ Deep Red dye (CTDR, dilution: 1/1000 for 10 min, C34565, Invitrogen) and CellMask™ Green Plasma Membrane Stain (1/1000 for 40 min, CMG, C37608, Invitrogen), respectively, to confirm the cellular localization after co-culture seeding of the vascularized stroma model. At the desired time point, matrices were fixed in 10 % formalin (F0046, Dia-Path, Italy) for 1 h at 4 °C under slight agitation, followed by permeabilization with 0.1 % Triton™ X-100 (Sigma-Aldrich) for 25–45 min at RT. Incubation with the primary antibodies (ABs) was done overnight at 4 °C. Briefly, endothelium was characterized by immunolabeling against CD31 while fibroblasts were labeled against Alexa Fluor® 555 CD90. ECM production and deposition by the FBs was investigated by staining against fibronectin (FN), collagen I and IV (Col I, Col IV) and laminin (Lam). Presence of intercellular junctions was verified by staining against VE-cadherin and ZO-1. Proliferation was studied by Ki67 labeling. Incubation with secondary ABs was carried out for 2 h at RT in the dark. List of primary and secondary ABs and dilutions used is reported in Table S1, Appendix. Morphological staining of actin filaments was performed by incubation in Phalloidin–Tetramethyl rhodamine B isothiocyanate (TRITC, 1/100–1/200, P1951, Sigma-Aldrich) or in Phalloidin, Fluorescein Isothiocyanate Labeled (FITC, 1/200, P5282, Sigma-Aldrich) for 1 h at RT in dark. Nuclei counterstaining with DAPI (4′,6-diamidino-2-phenylindole, dichlorhydrate, 1/2500–1/5000, D1306, Invitrogen™,) was done at RT for 1 h. Each step was followed by extensive rinsing (3×) in PBS 1X. Scaffolds were kept in fresh PBS 1X and stored in dark at 4 °C prior to imaging.

2.15. Clearing

Samples for lightsheet imaging were prepared by three different clearing protocols, after fixation and fluorescent immunostaining. For the first clearing protocol, 2,2′- Thiodiethanol (TDE,102428848, Sigma-Aldrich) was diluted in PBS 1X to created increasing gradient concentrations of 10 % - 30 % -50 % - 70 % - 90 % - 100 % (*v*/v%). Samples were incubated in each solution for 30 min at RT. Ethylcinnamate (Eci, 99 %, 112,372, Sigma-Aldrich) was used for a second clearing protocol, adapted from Masselink et al. (2019). [28] Briefly, increasing gradients of Eci were prepared by serial dilution in 1-Propanol (279,544, Sigma-Aldrich), with the same dehydration steps used for TDE, and the samples incubated for 30 min at RT. In the third protocol, the Urea-Based Amino-Sugar Mixture (UbasM) clearing protocol from Chen et al. (2017) was adapted. [29] Briefly, UbasM-1 (Ub-1) was prepared by mixing 25 % *w*/w% urea (15,604, Sigma-Aldrich), 25 % w/w% Meglumine (M813277, Shanghai Macklin Biochemical Co., China), 20 % w/w% 1,3-Dimethyl-2-imidazolidinone (40,727, Sigma-Aldrich), and 0.2 % w/w% Triton™ X-100 (Sigma-Aldrich) in MilliQ water. UbasM-2 (Ub-2) was prepared as a solution of 40 % w/w% sucrose (S9378, Sigma-Aldrich) 25 % w/w% urea and 20 % w/w% 1,3-Dimethyl-2- imidazolidinone in MilliQ water. Samples were incubated in Ub-1 for 1 h at RT, washed overnight in PBS at 4 °C and cleared with Ub-2 for 1 h at RT prior to imaging.

2.16. 3D imaging: detection of the collagen coating by second harmonic generation

The presence of collagen after coating was assessed by bi-photon (2P)-induced second harmonic generation (SHG, SP8, Leica Microsystems), equipped with a 405/10 nm bandpass. Samples were prepared by overnight immersion in PBS 1X and mounted on a plastic Petri dish by embedding in Aquasonic 100 ultrasound transmission gel (No. 01–08, Parker Laboratories, Inc., USA) to reduce light scattering. A 25× water immersion objective (HCX IRAPO, L25x/0.95, Leica) and excitation at 810 nm were used for image acquisition.

2.17. Confocal and AiryScan microscopy

3D confocal acquisitions were performed by using either a confocal TCS SP8 Leica microscope, equipped with an 25× water immersion objective (HCX IRAPO, 25×/0.95, Leica) or with a LSM 980 Zeiss microscope equipped with a 10× dry objective (EC-Plan Neofluar, 10×/0.3, Zeiss). The LSM 980 module AiryScan II was used for acquisitions using the AiryScan multiplex 4Y mode.

2.18. Macroscopy

Macroscopic images of the constructs were obtained with a Macro-Apotome (AxioZoom V16, Zeiss), equipped with a PlanNeoFluar Z 1× objective and a fluorescent lamp with adapted filter block (DAPI, GFP, DsRed, Cy5). Magnification tested for each sample were 8×, 40× and

80×.

2.19. Lightsheet microscopy

Lightsheet imaging was performed with the Alpha3 system (Phase-View, France), equipped with a 10× XL Plan N (XLPLN10XSVMP, Olympus, Japan) clearing objective with refractive index adaptive collar (RI 1.33–1.52) and a sCMOs Orca Flash4 camera (Hamamatsu, Japan).

2.20. Image reconstruction and analysis

Confocal and macroscope images were reconstructed and analysed using Fiji ImageJ (Java version 1.8.0) and ZEN Blue 3.5 (Zeiss). [30] Biphoton images were analysed with Imaris software (Bitplane AG, Switzerland). Airyscan and lightsheet images were converted in SIS Converter 3.1.1 and analysed with Vision4D 3.0.1 software (arivis AG, Germany).

2.21. Statistical analysis

Data have been reported as mean value ± SD. Statistical analysis was performed using Prism 7 (GraphPad Software, USA) and information on specific statistical tests have been provided for each dataset in the corresponding figure or table caption.

3. Results and discussion

3.1. Scaffold formulation and characterization

3.1.1. Formulations

The fabrication of the 3D porous scaffold containing inner tubular microchannels was performed by templating and cross-linking of a

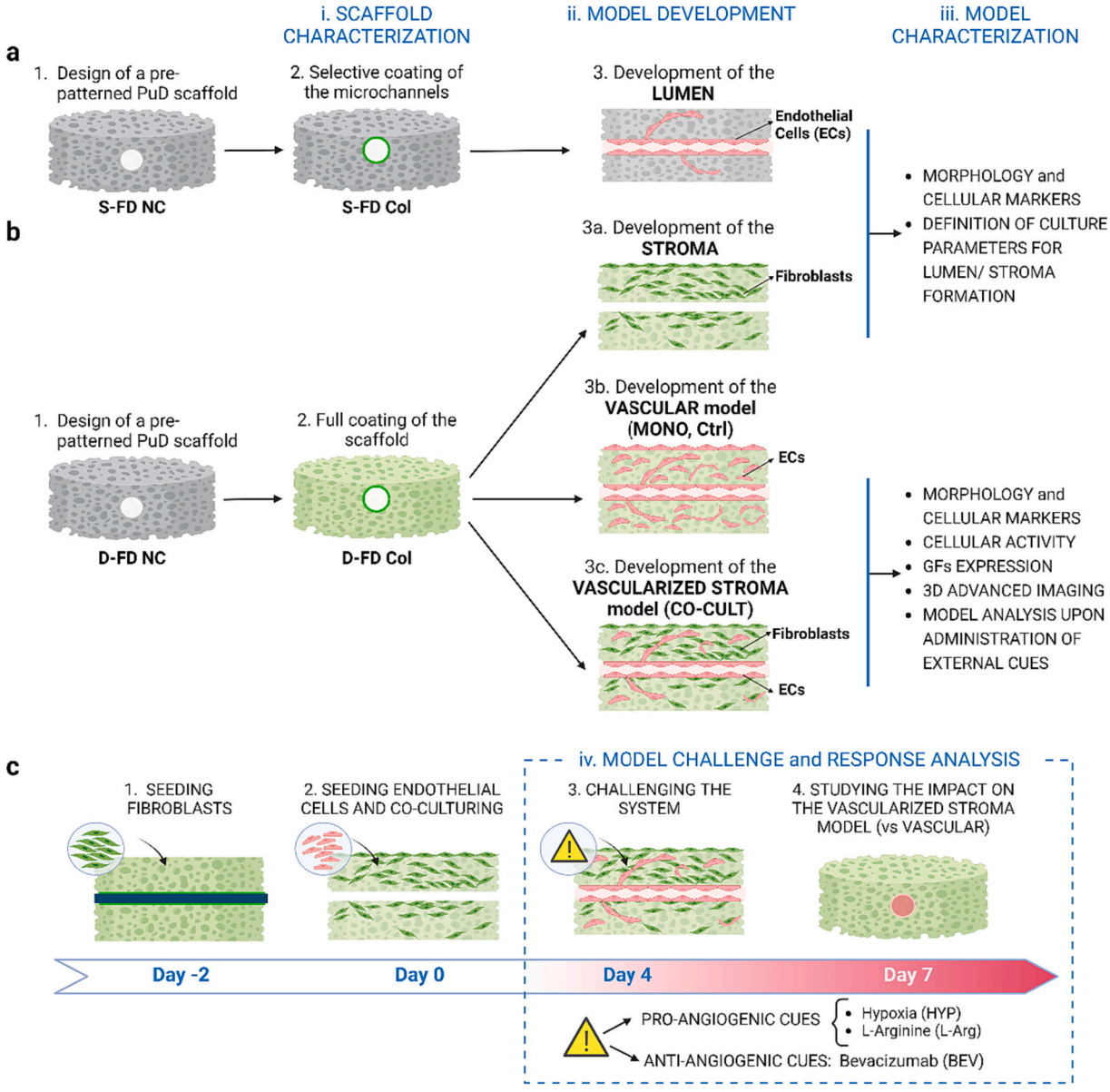

Fig. 1. Schematics showing the main steps reported in this work. (a,b) A pre-patterned pullulan/dextran (PuD)-based scaffold was used to create the vascular lumen (a3), and the stroma fraction (b.3a), separately. The protocols defined at this stage were used to develop the vascularized stroma model (CO-CULT, b.3c), while the vascular model (MONO, b.3b) was considered as negative control (Ctrl). The same PuD formulation could be used for both models by modifying the scaffold surface properties by addition of a collagen coating (green colour, S-FD Col and D-FD Col). (c) Insight on the co-culture model development steps and on the external stimuli applied to the system. Latin numerals (i-iv) represent the main steps of the models development and characterization. Created with Biorender.com.

water-soluble pullulan/dextran (PuD) polymers solution, followed by rinsing and freeze-drying (FD) to obtain the inner porosity. These biopolymers were chosen for their biocompatibility, manufacture versatility and for their GMP compliance, by adapting fabrication protocols patented by our group. [23,24,31,32]

The microchannels were obtained by molding the PuD hydrogel onto suture filaments, assembled within a custom-made 3D printed mold. [22] The spacers allowed to define the final scaffold's thickness and the gels were punched into cylindrical structures after cross-linking, with final dimensions after freeze-drying of 8 mm × 1–1.5 mm (diameter x height) and an inner channel of 100 μm in diameter upon hydration (Fig. S1, Appendix). To introduce cell adhesion moieties, a coating step with extracellular matrix (ECM) proteins was performed. Collagen from bovine corium at a concentration of 1 mg mL^{-1} was chosen upon optimization (data not shown), and two coating procedures were developed to obtain scaffolds with different localization of the protein (Fig. 1a,b). In a first protocol, the coating was performed before freeze-drying (S-FD Col), allowing the collagen to access only the open structures (namely the microchannels and the hydrogel edges). This formulation was used in the first steps of the project for the development and optimization of the lumen within the PuD hydrogels. To develop the stroma and the vascularized stroma models, a full coating procedure was performed: briefly, after a first freeze-drying, the scaffolds were re-hydrated in a bath of collagen solution and freeze-dried a second time (double freeze-drying, D-FD Col) upon collagen neutralization to ensure its presence within the microchannel, the matrix pores and onto the scaffold edges. These formulations were compared to their respective non-coated negative controls (NC) during scaffold characterizations, to investigate the modifications induced by collagen on the PuD. Fig. S2, Appendix, reports a detailed schematic of the formulations. The localization and structure of collagen was confirmed by second harmonic generation (SHG) imaging, that showed the coating of the microchannels only for the S-FD Col while the D-FD protocol permitted an overall coating of the PuD matrix (Fig. 2a,b). SHG images acquired during the filament removal confirmed that the collagen coating remained stable upon the scaffold hydration and removal of the template (Fig. S3, Appendix). Quantification of the collagen in the supernatant by BCA assay showed a higher content of collagen within the D-FD Col PuD, with a

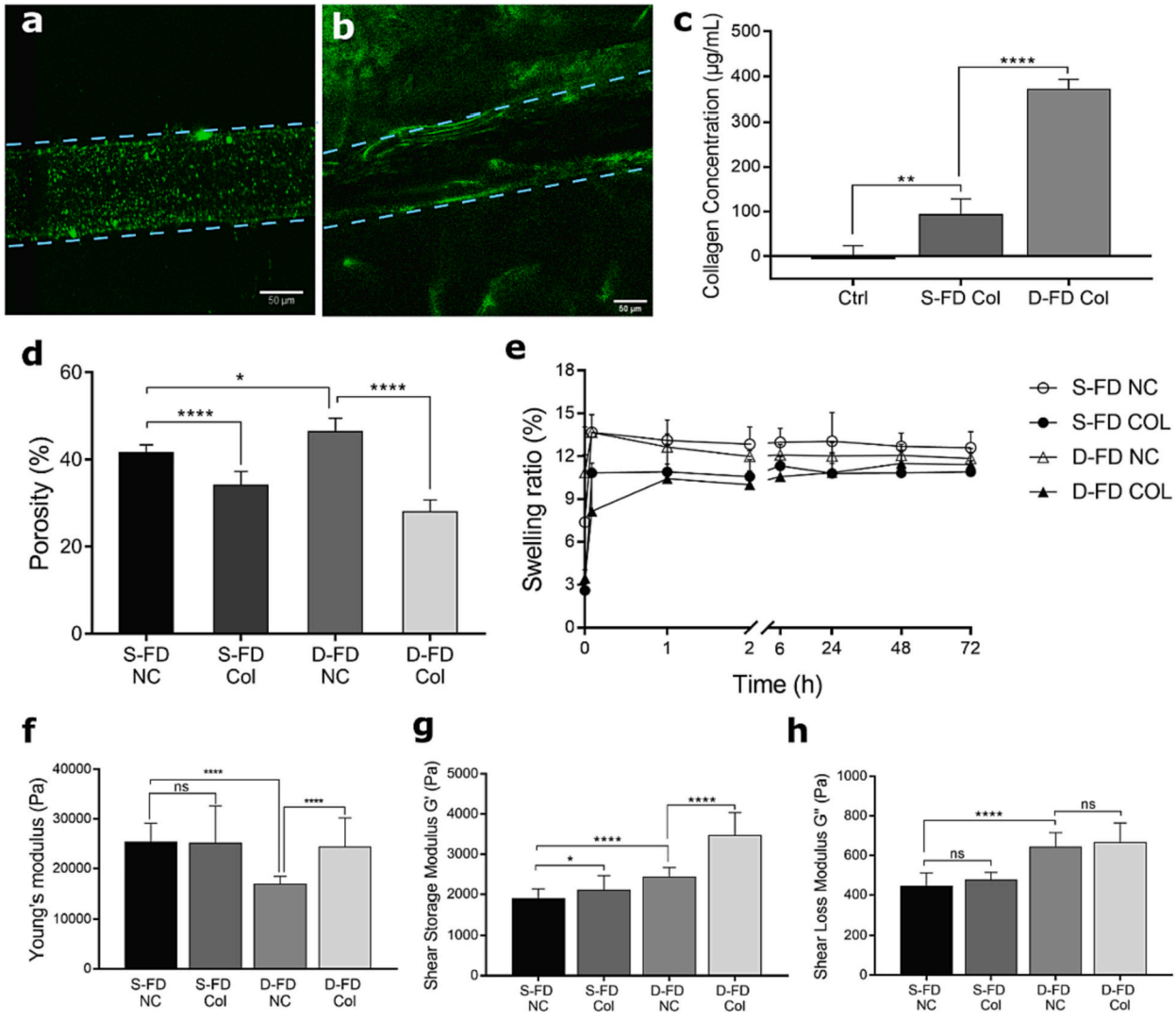

Fig. 2. PuD scaffolds characterization. (a,b) SHG images of collagen coating upon filament removal in the S-FD Col and D-FD Col formulations, respectively. Dashed light blue lines indicate the channel location. Scale bar: 50 μm. (c) Collagen concentration (μg mL^{-1}) calculated by BCA protein assay from supernatant readings for Ctrl (S-FD NC), S-FD Col and D-FD Col matrices. (d) Porosity (%), calculated by water squeezing method upon full hydration of the samples (2 h) and (e) swelling ratio (a.u.) over 72 h for the four scaffold formulations. (f) Young's modulus (Pa), calculated by nanoindentation on hydrated PuD scaffolds at D3. (g-h) Shear storage (G′) and loss moduli (G″) (Pa), calculated by rheometry on fully hydrated PuD scaffolds (48 h). Statistics: (c,d,f-h) One-way ANOVA with Tukey's post-hoc multiple comparisons test on each dataset separately (ns, not significant, *, *p*-value <0.05, ****, p-value <0.0001), (e) Two-way ANOVA with Tukey's post-hoc test; in the range 1 h–72 h, multiple comparisons test among the datasets showed ns, not significant.

concentration four times higher compared to the S-FD formulations (370.5 ± 22.32 μg mL^{-1} and 92.7 ± 35.36 μg mL^{-1}, respectively, Fig. 2c), coherent with the localization of the collagen coating in each formulation.

Despite the simple geometry of the vasculature obtained by subtractive molding, this method has been widely used to build vascularized 3D models, as it offers the advantages of high reproducibility, control of the manufacturing parameters, ease of fabrication and matrix handling. [33,34] As it permits the design of cylindrical 3D vessels and the modulation of their diameter, it enables researchers to overcome the limitations of other manufacturing approaches, such as soft lithography of microfluidic chips, that commonly determines rectangular cross-sections of the microchannels. [35] Furthermore, the arrangement of suture filaments in different layouts allowed us to fabricate PuD scaffolds with different channel patterns, as parallel or crossing structures (Fig. S1c, Appendix).

3.1.2. Physical properties

Measurements of total porosity and swelling were performed on the four formulations of freeze-dried scaffolds (S-FD NC, S-FD Col, D-FD NC and D-FD Col) to characterize their physical properties. Porosity was calculated by water squeezing method, as previously reported (Fig. 2d). [25] Data showed a reduction of the porosity percentage after coating of the constructs with collagen (41.51 % ± 1.86 *vs* 34.08 ± 3.15, 46.36 % ± 3.12 *vs* 27.98 % ± 2.68 for S-FD NC *vs* S-FD Col and D-FD NC *vs* D-FD Col, respectively), more noticeable for the D-FD Col formulation compared to the S-FD Col due to the higher collagen content (in line with the BCA results, Fig. 2c). Moreover, the second freeze-drying induced a slightly higher porosity (46.36 ± 3.12 *vs* 41.51 ± 1.86 for D-FD NC *vs* S-FD NC, respectively), due to additional pores created during the second freeze-drying.

Water absorption capability was studied by measuring the swelling ratio over the first 72 h of hydration. Within one hour, the swelling ratio reached a steady state, with values exceeding 10 times the original dry weight for all the formulations and only minor changes were recorded at 72 h (Fig. 2e). These results were in line with the porosity trends, and suggested a higher water uptake in absence of coating (NC) for both the single and double FD formulations, while no swelling trend was noticed by comparing the freeze-drying protocols. This behavior for collagen coated matrices might be in fact related to a reduced macroporosity due to the protein deposition, that caused a lower water intake, rather than being dependent on the freeze-drying step. The data from physical characterization were in line with findings previously published by our laboratory, that reported a porosity above 25 % and a swelling ratio in a range of 10–14, confirming consistent protocols reproducibility for the fabrication of PuD matrices. [20,36] Published models of pullulan-based matrices have also reported similar values for physical properties. [37–39]

3.1.3. Mechanical properties

Nanoindentation and rheometry measurements were performed to assess the micro and macro mechanical behavior of the PuD matrices after hydration in PBS, respectively. Results from nanoindentation showed a constant stiffness of the surface of about 25 kPa for the formulations S-FD NC, S-FD Col and D-FD Col while a lower stiffness of D-FD NC was observed, being of 16.86 kPa ± 1.56 kPa (Fig. 2f). The results suggested that the double freeze-drying procedure was responsible for a decrease of the surface stiffness, in line with the porosity trends, that showed a higher porosity of DFD-NC compared to SFD-NC. Consistently, the collagen coating induced a decrease of the porosity and an increase of the Young's modulus compared to the non-coated scaffold, suggesting that the collagen fibers filling the matrix pores were responsible for the modification of both physical and mechanical properties of PuD matrices.

Fig. S4, Appendix reports the Young's modulus trend over time. The S-FD NC, D-FD NC and D-FD Col formulations showed an increase of the stiffness over the first three days with a peak at Day 3, followed by a decrease for longer hydration time and values at D7 below 15 kPa. The S-FD Col condition stands out with a doubling of the Young's modulus observed at Day 7 (30.66 kPa ± 2.69 kPa), suggesting a delayed peak of stiffness compared to the other formulations, a behavior that might be attributed to the different rearrangement mechanism of collagen fibers.

Results from rheometry experiments showed an increase of the shear storage modulus G′ after both coating and D-FD steps (Fig. 2g). The presence of collagen in S-FD matrices entailed an increase of the stiffness from 1.9 kPa to 2.1 kPa while the D-FD increased G′ up to 2.4 kPa in absence of coating. The highest G′ was reported for the D-FD Col formulation, with a value of 3.5 kPa. The shear loss modulus G″, representative of the viscous behavior, was not affected by the presence of collagen (no statistical difference between the NC and Col formulations), while it increased after the D-FD procedure, with a G″ up to 0.6 kPa for the D-FD Col samples, compared to values below 0.5 kPa for the S-FD formulations (Fig. 2h).

The comparison between the nanoindentation and the rheometry results underlined a different mechanical response of the PuD matrices when the surface or the bulk properties were investigated: while the bulk properties showed a maximal stiffness below 3.5 kPa for the D-FD Col matrices, the surface values by nanoindentation mostly revealed the stiffness sensed at the microscale by cells (tip radius of the indentation probe of about 100 μm), with values between 13 and 30 kPa.

These results enlighten the importance of evaluating the mechanical properties of TE constructs by use of complementary techniques to determine the multiscale mechanical behavior of the biomaterial before its biological application.

As the onset of many diseases is correlated with stroma remodeling and variation of tissue stiffness (normally an increase, as in the case of tumor microenvironment-related changes), biomimicry of biomaterials mechanics plays a crucial role for TE development. [40]

Results from bulk characterization are comparable to the stiffness of living soft-to-medium tissues calculated from strain-stress analyses, reported to be below 10 kPa, and showed consistency with previously reported works on pullulan scaffolds. [38] At a cellular level, AFM studies previously reported that fibroblasts mechanical moduli can reach 30 kPa, a value similar to the results we obtained by nanoindentation. [41] These findings allowed us to validate our D-FD Col scaffold formulation for consecutive *in vitro* modeling of the vascularized stroma.

3.2. Optimization of vascular and stroma culture parameters

3.2.1. Development and characterization of the vascular lumen compartment

A functional and perfusable lumen was developed by seeding ECs within S-FD Col PuD scaffolds. ECs concentrations ranging from 1×10^6 to 5×10^6 cells mL^{-1} were tested and the results evidenced the possibility to tune the lumen formation over time, with ECs patterning the channel in a variable time between 4 and 11 days. As a proof of concept for the design of more a complex vascular model, parallel lumens were engineered by using matrices containing multiple molded microchannels (Fig. S5, Appendix). An optimal ECs concentration of 2×10^6 cells mL^{-1} was identified, with morphological analyses of the lumen showing the elongation and alignment of the ECs cytoskeleton (staining of F-actin), even in absence of flow (Fig. 3a). Expression of CD31/PECAM-1 and vascular endothelial (VE)- cadherin confirmed the physiological-like behavior of the endothelium and the functional adhesion of cells assembling the lumen (Fig. 3b). [42,43] Upon lumen formation, sprouting within the S-FD Col matrix could be observed, suggesting the capability of the vessel to initiate a spontaneous angiogenesis in absence of adhesion moieties (collagen coating in the microchannel only, Fig. 3c). Indeed, ECs from different origins have been previously demonstrated to actively synthetize ECM proteins, as collagen type I, during sprouting. [44] We believe that more consistent

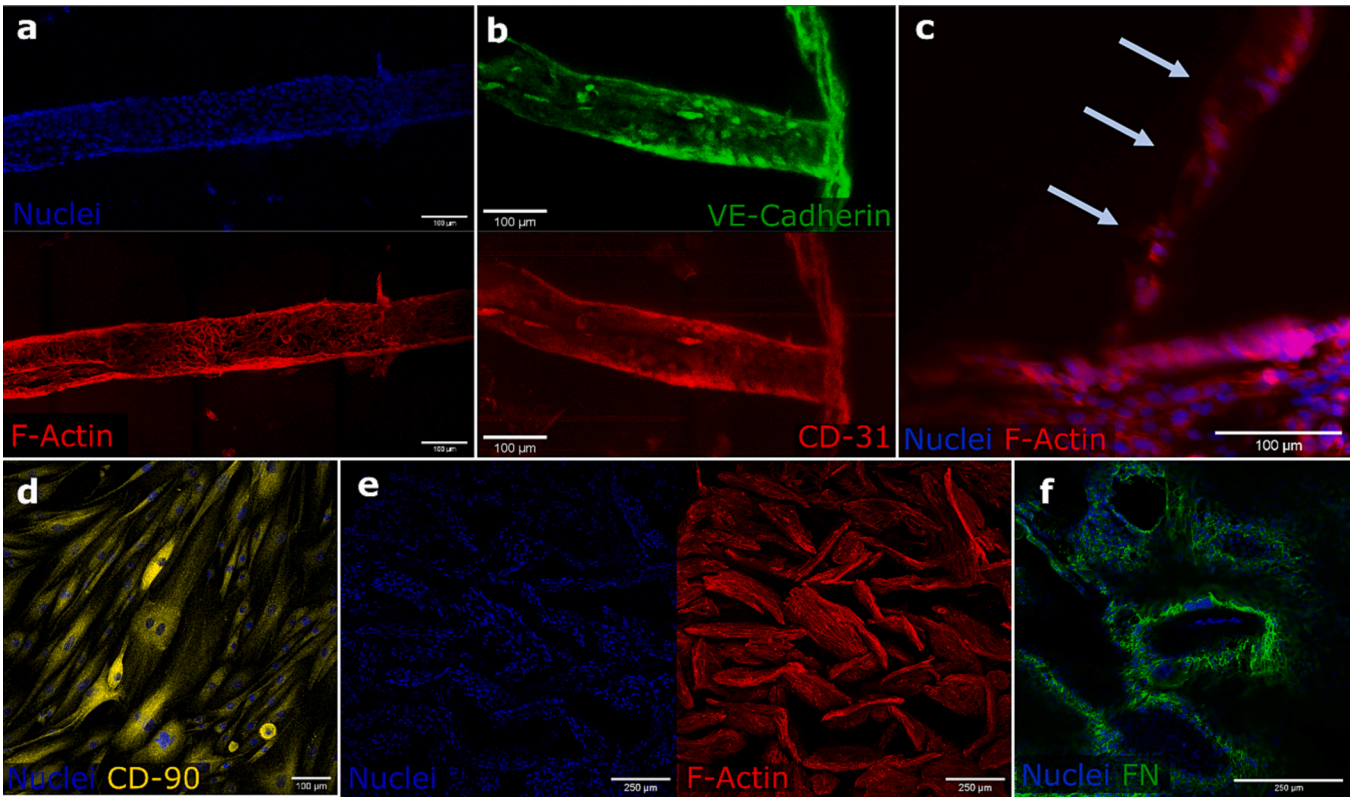

Fig. 3. Investigation of the vascular (a-c) and stroma (d-f) monocultured models. (a) 3D rendering of the lumen obtained by seeding of 2×10^6 HUVECs mL^{-1}, imaged at Day 7 (staining with DAPI, blue and phalloidin, red) by bi-photon microscopy. (b) Confocal image of the channel inlet, stained against VE- cadherin (green, top) and CD31 (red, bottom). (c) Representative confocal image of sprouting from the main channel (light blue arrows). (d) Staining of fibroblasts cultured in 2D by Alexa Fluor 555 CD90 (yellow). (e) Colonization of the PuD matrix's pores at Day 4 by the fibroblast fraction (staining with DAPI, blue and phalloidin, red). (f) Scaffold surface at Day 7: fibroblasts (DAPI, blue) line and fill the matrix pores and produce fibronectin (FN, green). Field of View (FOV): central section of the microchannel (a,c), edge of the microchannel (b), matrix pores (e), matrix surface (f), top views. Scale bars: 100 µm for (a-d), 250 µm for (e,f).

sprouting from the main channel within the matrix pores could be obtained by enhancing the scaffold porosity, for instance by increasing the porogen content. [20] Nevertheless, modifications of the scaffold formulation should be investigated carefully to preserve the chemical and mechanical properties needed for consecutive *in vitro* application.

3.2.2. *Development and characterization of the fibroblastic stroma compartment*

The development of the stroma microenvironment required a full coating of the scaffold to obtain D-FD Col matrices necessary to prevent the fibroblast fraction to form spheroids within the pores. D-FD Col matrices were seeded with human neonatal skin fibroblasts and the stroma fraction was characterized by positive staining with CD90/ Thy-1, a mesenchymal and fibroblast surface marker (Fig. 3d). [45,46] Fibroblasts localization and morphology were investigated upon scaffolds seeding, showing their adhesion to the pore walls and their capability to homogeneously proliferate, assuming an elongated morphology aligned with the pore's major axis direction (Fig. 3e). These observations were coherent with previous works focused on the cellular behavior within anisotropic scaffolds, that showed how the presence of oriented structures determined increased proliferation, preferential orientation of cells and differentiation towards a specific phenotype thanks to the matrix guidance cues. [47,48] The results enlightened the fundamental role of scaffold's micro and macroarchitecture in determining cellular response. For culturing times over 7 days, formation of detachable cell sheets onto the matrix surface could also be observed, indicating the fibroblasts capability to create stable intercellular junctions and to self-assemble into 2D sheet tissues (Fig. S6a, Appendix). [49] Analysis of ECM matrix over time confirmed a sustained production of fibronectin (FN), laminin (Lam), collagen (Col) IV and Col I, that layered the whole matrix structure and reshaped its surface and core (Fig. 3f, Figs. S6b-e and S9d, Appendix). Coherently with fibroblasts alignment, an oriented distribution of FN and Lam could be observed along the pores walls and on the scaffolds surface. For Col IV and Col I, the formation of fibers and a hierarchical organization was noticed at Day 7. Mechanical characterizations of the stroma at Day 7 indicated an increase of the Young's modulus compared to unseeded scaffolds from 14.5 kPa to 18.3 kPa as well as of the viscous bulk behavior (G'' from 0.6 kPa for the control *vs* 0.9 kPa for the seeded scaffolds) while a 10 % decrease of G' was observed (Fig. S7, Appendix). We believe that this trend could be mostly attributed to the ECM deposited, that caused a higher rigidity at the microscale and an overall increase of the scaffold viscosity. [50] Secretion of enzymes, as matrix metalloproteinase-2 (MMP-2), is known to be a driving mechanism for both *in vitro* and *in vivo* degradation of scaffolds. Our results from MMPs analysis reported below for the stroma model could therefore explain the decrease of the storage modulus at the macroscale. [51]

3.2.3. *Development and 3D imaging of the vascularized stroma model*

To determine the maximum seeding density, proportional to the maximum liquid intake of the biomaterial, D-FD Col scaffolds were used to create a mono-culture model of ECs (MONO, with endothelial cells in the microchannel and in the pores), considered as negative control of the heterotypic model. Results showed that for concentrations above 5×10^6 cells mL^{-1}, cells reached a confluent state within few days, followed by a fast apoptosis and, ultimately, a failure of the cellularized construct.

The co-culture model was developed by optimizing the cells ratio, cell culture media ratio and seeding protocols. The adoption of a dual step seeding procedure enabled us to build a functional vascularized stroma model (Fig. 1c). Fibroblasts were seeded by dropping to a final

density of 3×10^6 cells mL^{-1} and by maintaining the suture filament in place to prevent their access to the channel. After 48 h, ECs at optimal concentration of 2×10^6 cells mL^{-1} were added by syringe vacuum after filament removal. Fluorescent images of pre-stained cells confirmed their proper localization within the scaffold structure by using the optimized dual step protocol (Fig. 4a): fibroblasts pre-stained with CTDR, could be observed on the surface of the scaffold, lining the matrix's pores, while ECs, pre-stained with CMG and seeded after the filament removal, were localized within the matrix channel. Analysis of fluorescence images at Day 7 of co-culture revealed a sustained expression of *zonula occludens -1* (ZO-1), produced by both cell types, that confirmed the formation of intercellular tight junctions (Fig. 4b). Immunostaining with the endothelial markers CD31 and von Willebrand factor (vWF) allowed to distinguish the two cell types after seeding and to study their mutual localization. Results confirmed colonization of matrix microchannels and lumen formation by ECs (Fig. 4e,f) and evidenced their presence on the surface as well (Fig. 4c,d). Nonetheless, a systematic morphological analysis was hampered by the challenge of imaging the 3D model. In fact, tissue engineers nowadays are facing the major challenge of preserving the 3D information carried by complex TE models while obtaining meaningful results. [52,53] In the stroma-containing models, the high cellular density and the ECM deposition made the scaffold opaquer with time, thus hampering an in-depth analysis of the microstructures. While histological procedures for tissue sectioning have been adapted to biomaterials, these protocols often entail a deformation of the biomaterial during sectioning, as in the case of PuD matrices, creating a potential misinterpretation on the 3D cellular arrangement and biological behavior. [54] We thus decided to avoid sectioning to preserve the scaffolds 3D structure, morphology and cellular information and to perform in-depth parallel imaging *via* confocal AiryScan, bi-photon and light-sheet microscopy (LSFM). As some of these techniques requires sample clearing, we conducted side studies to clear the stroma samples by adaptation of tissue clearing protocols to the PuD scaffold (Figs. S8 and S9, Appendix). Few works have been reported on optical clearing of biomaterials-based 3D models, mostly by hydrophilic procedures, such as by use of FocusClear reagent or *via* hyperhydration with CUBIC. [55,56] Nonetheless, optical clearing of biomaterials remains largely unexplored and, to the best of our knowledge, no data have been reported for pullulan-based scaffolds. [57]

Here, we modified the hyperhydration protocol based on use of Urea-Based Amino-Sugar Mixture (UbasM) from Chen et al. (2017) to obtain an acquisition depth up to 900 μm, thus increasing the imaging depth by a four-fold factor compared to uncleared samples. [29,58] Our results enlighten the need for further developing optical clearing and volumetric imaging of TE models to unveil their 3D structure and the model behavior. Taken together, we believe that this strategy opens up new ways to develop clearing procedures for biomaterials and for three-dimensional visualization of thick TE constructs.

3.3. *Vascularized stroma response to external stimuli: Viability, morphology, cell markers and permeability studies*

The vascularized stroma model (CO-CULT) was subjected to different

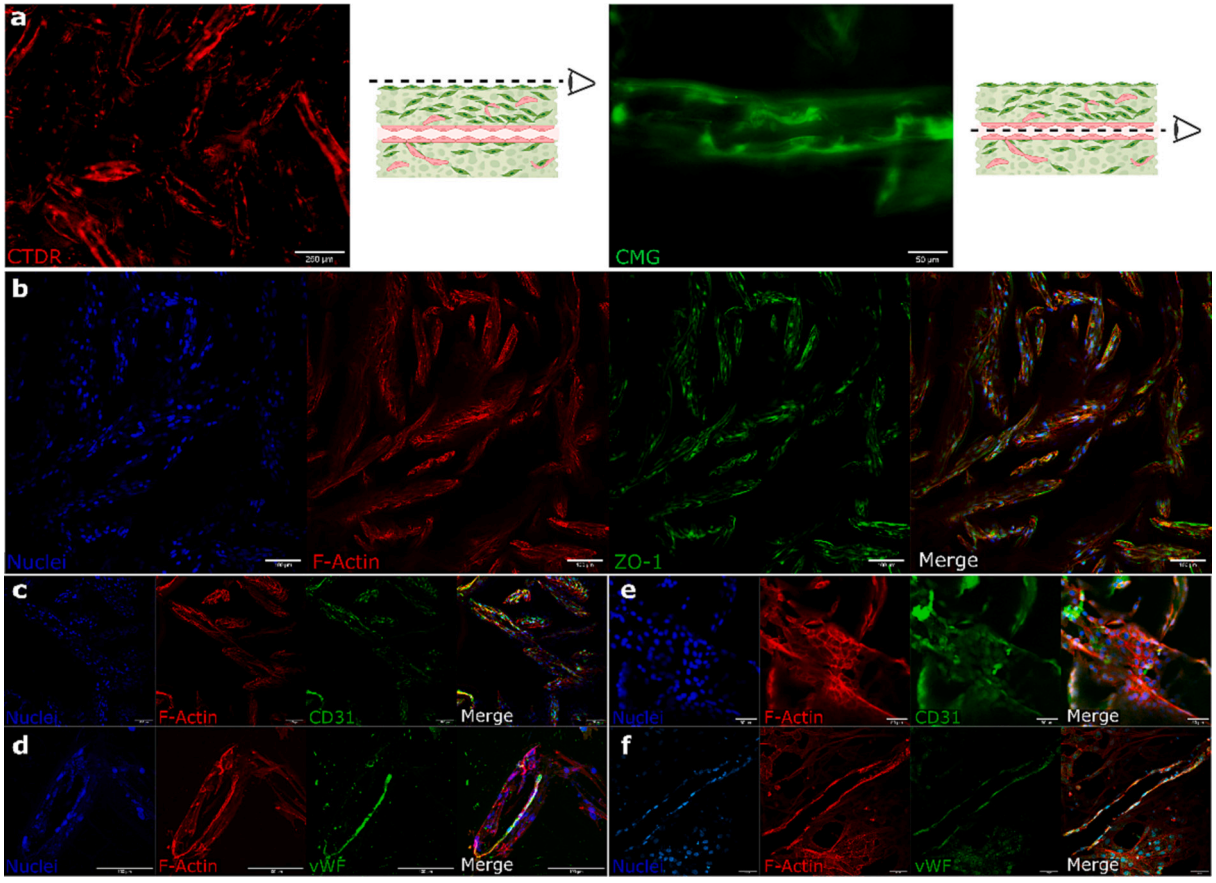

Fig. 4. 3D vascularized stroma model fabrication and co-culture markers. (a) Cellular localization after double-step co-culture seeding: fibroblasts (CTDR, red) were located on the matrix surface (left) while ECs (CMG, green) were found within the channel two hours upon seeding (right). Schematics of the matrix indicate the observation area. Images taken with an optical microscope 2 h after each seeding step. Scale bars: 250 and 50 μm, respectively. (b-d) Surface images of cells stained against ZO-1 (both types), CD31 and vWF (ECs), respectively. (e,f) Microchannel images of ECs stained against CD31 and vWF (ECs), respectively. Nuclei (DAPI, blue) and actin (phalloidin, red) represent cell location and morphology. FOV: central section of the microchannel (a-*right*, e,f), matrix pores (a-*left*, b-d), top views. Scale bars: 100 μm. (c,d) and 50 μm (e,f).

external stimuli, known to mainly affect the angiogenesis process and the ECs fraction, and its response compared to the ECs monoculture (MONO) vascular model, with the objective of studying how the fibroblasts mediate the vascular response to external cues. In this context, three parallel studies were conducted to expose the models to (i) hypoxia (1 % O_2), (ii) 1 mM L-Arginine or (iii) 0.1 mg mL^{-1} bevacizumab, the hypoxia percentage and the molecules concentrations being chosen based on published studies. [59–61]

The hypoxic condition, defined as an oxygen level below 5 %, was chosen as pro-angiogenic cue. [62,63] While the role played by VEGF has been largely studied in both 2D and 3D vascular models, we decided to consider in parallel the role of nitric oxide (NO) to evaluate angiogenic effects. NO, produced by cells as free radical, is known to participate in regulation of blood pressure, cellular homeostasis, inhibition of platelet aggregation and during angiogenesis, notably by activation of the cyclic guanosine monophosphate (cGMP) pathway. Furthermore, a mutual interaction between NO and VEGF occurs in VEGF-mediated angiogenesis. [64,65] In pathological conditions, when the angiogenesis is unbalanced, the NO production is altered. Though some works have investigated the NO response of 3D *in vitro* models during angiogenesis, its role is largely overlooked. [5,66] Here, we have investigated the NO production and correlated it to the VEGF expression.

As NO is mainly produced from L-arginine (L-Arg) conversion, we investigated in a second study the responsiveness of the model by supplementing the cell culture medium with 1 mM L-arginine. [5,67,68] This amino acid has been administered as dietary supplement to patients and its effects studied on a plethora of pathologies, including cardiovascular diseases (atherosclerosis, hypercholesterolemia, pre-eclampsia), diabetes, neurological pathologies, as dementia, and cancer. [69]

In a third study, we investigated the response of the vascularized stroma tissue to an anti-VEGF drug, bevacizumab (BEV), commonly used for targeted therapy of colorectal, breast, ovarian and non-small-cell lung cancer, glioblastomas, and retinopathies, here administered at 0.1 mg mL^{-1}. [70,71] Preliminary experiments were carried on the monoculture model to choose the BEV concentration and administration window (Fig. S10, Appendix).

All the treatments were administered independently at Day 4 of co-culture for 3 consecutive days and the model response monitored over 72 h. Viability studies performed by LDH assay at Day 7 indicated a higher mortality for the monoculture model for all the tested conditions (Ctrl mono 49.7 % *vs* Ctrl co-cult 31.6 %, Fig. 5a). The co-culture model under challenge did not show any significant mortality increase over 7 days, with values always below 30 %. The results were confirmed by Live/Dead staining (Fig. S11, Appendix), that did not indicate a significant cellular apoptosis upon vascularized stroma treatment.

Images of cell localization and morphology by Calcein AM and phalloidin staining, respectively, did however show a reduction of the cell number in the pores compared to the control, notably for L-Arg and BEV treatments, and partial changes of cellular cytoskeleton (Fig. 6a). Particularly, BEV administration induced a modification of the cells spindle shape into a more irregular one, with cells assuming a broader conformation and developing ruffles at the edges. Comparison of cellular morphology underlined that the presence of fibroblasts helped in preserving the cell shape, as no rounded apoptotic cells were noticed in the vascularized stroma tissue (Fig. S10).

In the monoculture model, neither the hypoxic nor the L-arginine conditions induced a higher cytotoxicity compared to the control, while

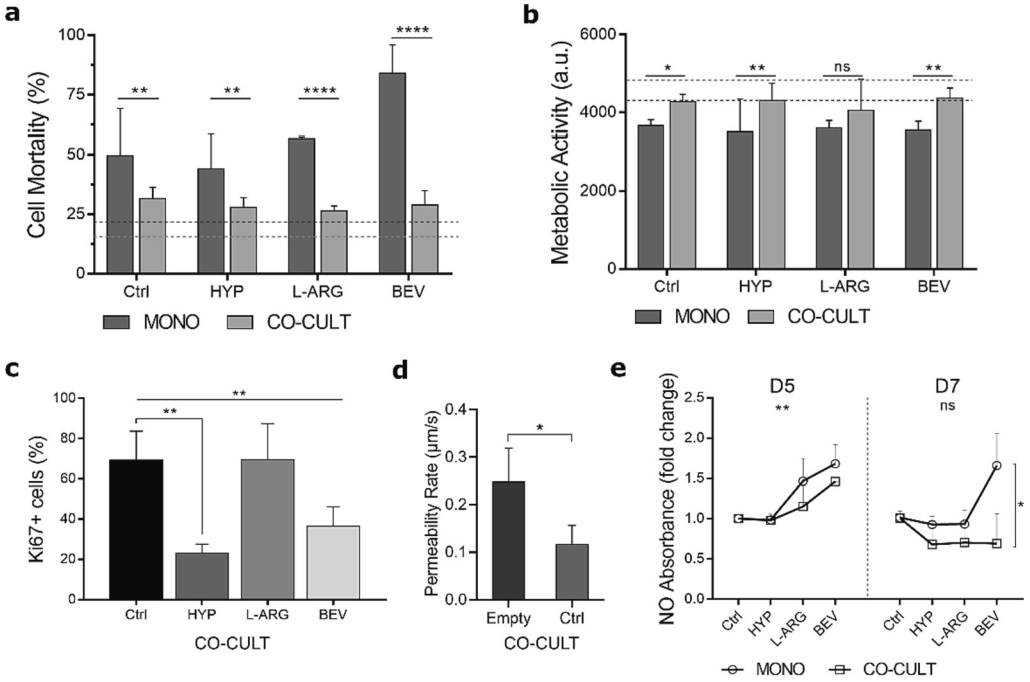

Fig. 5. Quantitative analyses of cellular behavior for the vascular and the vascularized stroma models upon stimuli administration. (a) Cell mortality rate (%) calculated by LDH assay at Day 7 for the monoculture vascular and co-culture vascularized stroma models, either untreated (Ctrl) or exposed to the cue for three days (HYP, L-Arg or BEV). Dotted lines represent the average mortality rate before any treatment (Day 4 of culture) for the monoculture (black line, average mortality 21.88 % ± 6.53 %) and the coculture (gray line, average mortality: 16.15 % ± 6.53 %), respectively. (b) Cell metabolic activity (a.u.) calculated by Resazurin assay at Day 7 for monoculture (ECs only) and co-culture matrices, either untreated (Ctrl) or exposed to the cue. Dotted lines represent the average metabolic activity before any treatment (Day 4 of culture) for the monoculture (black line, average metabolic activity 4290.03 ± 771.40) and the coculture (gray line, average metabolic activity: 4820.61 ± 646.88), respectively. (c) Ki67-positive cells (%) in the CO-CULT model, calculated on selected ROIs as ratio of positive cells compared to the total number (DAPI staining for nuclei counting). (d) Permeability rates (μm s^{-1}) calculated at Day 7 for empty and untreated co-cultured scaffolds (Ctrl). (e) NO absorbance at 540 nm at D5 and D7 of culture, expressed as fold change of each Ctrl at D5. Statistics: (a,b-e) Two-way ANOVA with Bonferroni's post-hoc test to compare the two datasets (ns, not statistically significant, *, *p*-value <0.1, **, p-value <0.01, ****, p-value <0.0001), (c) One-way ANOVA with Tukey's post-hoc test (*, $p \leq 0.05$, **, p-value <0.01), (d) Unpaired *t*-test, $p = 0.0492$, *, $p \leq 0.05$.

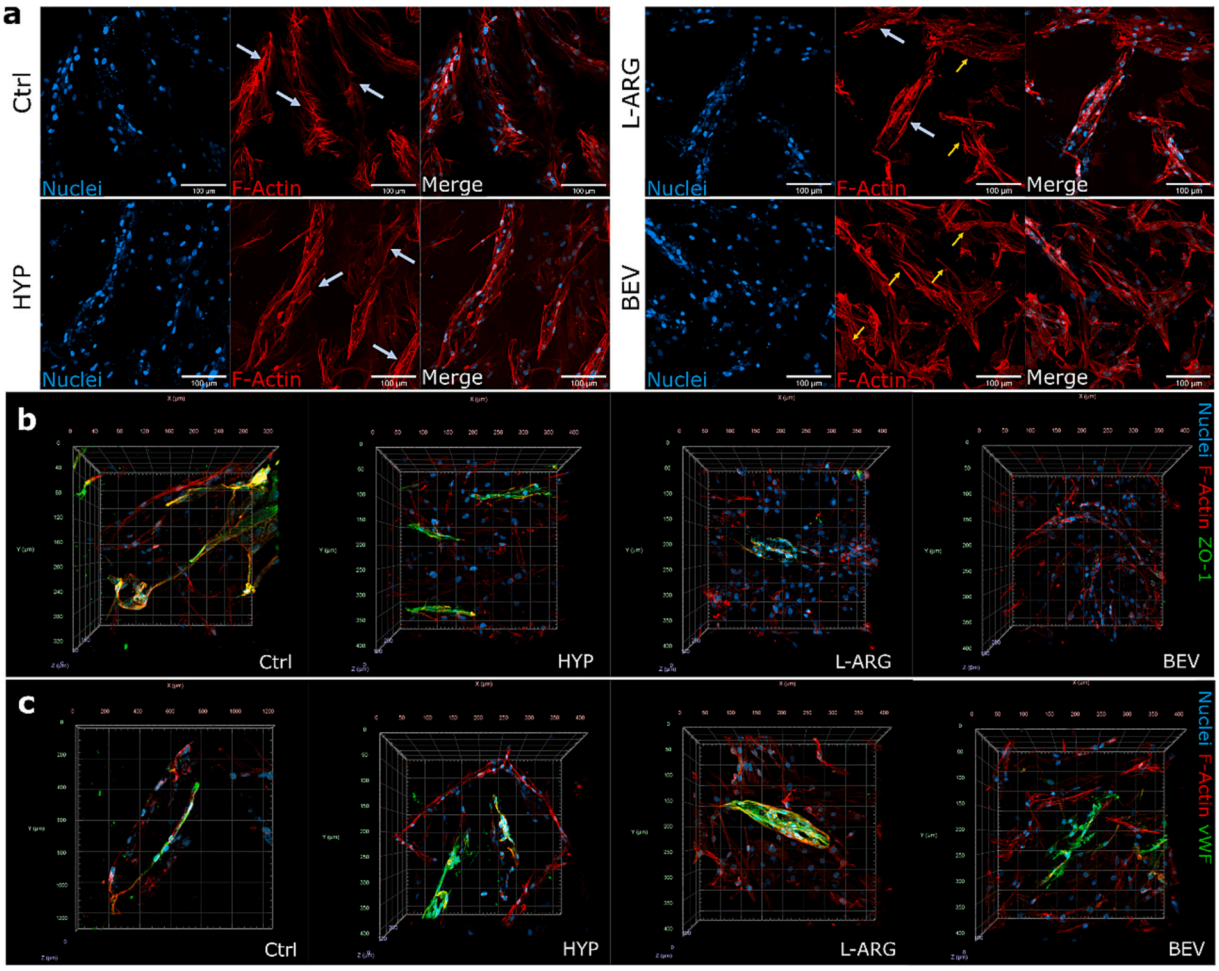

Fig. 6. 3D vascularized stroma model characterization upon treatment. (a) Cellular distribution and morphology (nuclei, blue and F-actin, red, right: merged image) for the control and the three conditions tested. Light blue arrows indicate oriented F-Actin stress fibers, yellow arrows indicate aberrant protrusions and spread cell morphology. Scale bar: 100 μm. (b-c) 3D arivis rendering of vascularized stroma at Day 7 upon treatment. Staining for ZO-1 (b) and vWF (c), as vascular marker. FOV: (a-c) matrix pores, top views. Images acquired by Airyscan.

the administration of BEV at 0.1 mg mL^{-1} impacted significantly the ECs viability and morphology, with an overall average mortality over 80 % and conversion of cells to a round shape (Fig. 5a). Similar results of mortality on ECs 3D models have been reported for same concentrations of other cancer targeting drugs, as bortezomib in a range of 0.1–1 μM. [72] In our study, preliminary assays performed on ECs monoculture at different BEV concentrations (0.1 and 0.5 mg mL^{-1}) did not indicate a dose-dependent response. When administrating the drug for 1 h, followed by withdrawal over 3 days, as similar to clinical protocols, only partial benefits were observed compared to longer administration windows (notably, recovery of NO and VEGF production). However, viability data suggested a triggered mechanism of apoptosis and the incapability to recover upon BEV administration. These first experiments allowed us to establish the drug concentration used in this study (0.1 mg mL^{-1}) and an administration window of 72 h, as in the case of the pro-angiogenic stimuli.

Results from the metabolic activity were consistent with the viability studies, showing reduced cellular metabolism for the vascular model, with no statistically significant difference among the conditions tested (Fig. 5b).

Cell proliferation within the matrix pores, assessed with nuclear Ki67 marker staining, revealed that the untreated condition showed almost 70 % of Ki67+ cells, similarly to L-Arg treatment, while proliferation was reduced in hypoxic and BEV conditions (23.1 % and 36.3 %, respectively) (Fig. 5c). For both hypoxia and L-Arg treatments, a major proliferation was observed at the surface of the scaffold, with Ki67 positive cells forming an adhesive monolayer onto the PuD. Nonetheless, the Ki67 expression at the surface was not representative of proliferation rates within the matrix core, therefore the surface area was not taken into account for the quantitative analysis reported here. Proliferation has been previously reported to be inhibited under hypoxia conditions for multiple cell types, including fibroblasts. One of the main mechanisms suggested is the action of the hypoxia-inducible factor 1 (HIF-1), a transcription factor responsible of oxygen-dependent cellular modifications and of angiogenic growth factors transcription in endothelium. [73] As upregulation of HIF-1 has been previously shown to reduced stroma proliferation by arresting the cell cycle, we would suggest a further investigation of HIF-1 influence over 3D heterotypic cultures to verify the consistency with reported studies on 2D, 3D and *in vivo* models. [74–78] For BEV condition, the decrease in Ki67+ cells in a dose-dependent manner has been reported for *in vivo* models. [79] Finally, data from perfusion of empty (unseeded) microchannels and vascularized stroma tissue with FITC-conjugated dextran (70 kDa) confirmed the barrier function exerted by the vasculature, as the model showed a halved permeability rate compared to the control (Fig. 5d).

3D analysis of cellular markers distribution revealed expression of ZO-1 in hypoxic condition and L-Arg administration, mainly observed in the superficial area of the model and lining the matrix pores margins (Fig. 6b), while BEV treatment induced a loss of ZO-1 marker. In a work conducted onto retinal epithelial cells, a 48 h BEV administration

induced a reduced ZO-1 gene expression and an upregulation of mesenchymal markers, with a morphological transition towards a fibroblastic-like phenotype. [80] In further studies, analysis of other mesenchymal markers, as alpha- smooth muscle actin (α-SMA), could be envisioned to better understand the fibroblasts genetic response to these cues.

Staining of the vascular fraction for vWF showed a major presence of ECs within the pores, especially for L-Arg treatment, while no significant differences in vWF expression were observed for hypoxia and BEV administration (Fig. 6c). Similar results were obtained for VE-Cadherin expression (data not shown). The images were confirmed by quantitative vWF cytokine analysis (Table 1). We believe that the increased EC marker expression within the surface pores under L-Arginine, consistent with Ki67 results, could be attributed to two differential mechanisms: (i) proliferation of the ECs that firstly adhered to the surface during the seeding, or (ii) migration of ECs from the core of the matrix towards the surface or a combination of both mechanisms. Experiments as live cell tracking should be conducted to further decipher the model reshaping during stimuli response. Taken together, we concluded that ECs showed a dynamic behavior modulated by the fibroblasts upon treatment.

3.4. Differential interaction of VEGF and NO in the vascular and vascularized stroma models

Results of NO detection showed an increase of NO release at Day 5 (24 h administration) upon either L-Arg or BEV stimuli for both the vascularized stroma model and the control (Fig. 5e). The increase of NO upon L-Arginine was followed by an increase of VEGF over 72 h for the vascular fraction, coherently with previous studies, that showed augmented NO levels in endothelial cells and subsequent VEGF production, mainly *via* HIF-1 activity. [65,81]

Readings of NO levels under BEV stimulus showed that the vascularized stroma model had peak of NO at Day 5 and then returned to basal values at Day 7, with a concentration below 5 μM (close to physiological values), while the monoculture exhibited a sustained release of NO along the entire administration period. [65]

A major reduction of VEGF expression was coherently observed for the BEV conditions, with a drop from about 1 μg mL^{-1} to 20 pg mL^{-1} (Table 1).

Previous works showed that fibroblasts survival and NO production were not affected upon a 5 days treatment of BEV 0.1 mg mL^{-1}. In other *in vivo* models and clinical works, NO has been demonstrated to decrease after BEV administration, while experiments performed *in vitro* showed increased NO levels for higher BEV doses. [61,82,83] Although some works have studied the effect of anti-VEGF therapeutics on endothelial monocultures, showing impaired vascular features and anastomosis, limited studies are available on this drug class on 3D heterotypic models. [84,85] Based on literature, the expected behavior for our model would have been a drop of NO values in response to BEV anti-VEGF action. Interestingly, these results showed an impaired response mechanism in the first 24 h of BEV administration, suggesting that NO upregulation does not depend solely on VEGF-activated pathways and that a downregulation of VEGF in response to BEV did not translate directly into a NO drop. We believe that the upregulation of NO might be connected to an increase of oxidative stress and ROS production. [86,87] Furthermore, as the co-culture model was capable of re-establishing NO levels at 72 h, a complex response mechanism to BEV might be mediated by the fibroblasts compared to the vascular fraction alone, consistently with an increase of VEGF concentration. On the opposite, NO levels remained impaired in the vascular model over the 72 h, despite an increase in VEGF levels, confirming the presence of differential pathways in mediating endothelial NO response (Fig. S12, Appendix). Though further analyses should be performed to better understand the NO-VEGF interactions, such as readings of ROS levels or administration of NOS inhibitors, as N(G)-nitro-L-arginine methyl ester (L-NAME), these findings suggest the possible use of this vascularized stroma model as platform for investigating the response to drugs of a complex 3D heterotypic environment. The results also underlined the limitations of deciphering such responses to external stimuli by adopting monoculture models and reiterated the importance of developing relevant multicellular models for 3D *in vitro* studies. Overall, these results confirmed the positive effect of the stroma in mediating the endothelium NO response under both pro and anti-angiogenic cues.

Table 1
Concentrations of cytokines (pg mL^{-1}) obtained by Luminex Protein Assay for the mono and co-culture models at Day 7 in basal conditions (Ctrl) and upon challenge (HYP, L-Arg, BEV, $n = 2$).

Concentration (pg mL^{-1})						
Condition		CD31	bFGF	VEGF	IL-8	vWF-A2
MONO	Ctrl	625.4	52.87	1548.91	1131.67	37.16
	HYP	363.47	55.86	1114.68	519.98	42.34
	L-ARG	716.24	66.44	1854.79	1246.21	35.83
	BEV	< 350	77.31	28.35	820.43	34.47
CO-CULT	Ctrl	826.55	52.69	1087.17	3513.17	28.87
	HYP	625.4	44.63	832.91	3331.43	27.42
	L-ARG	744.83	43.89	881.29	3922.92	56.8
	BEV	< 350	42.66	20	3430.36	39.78

3.5. Protective role of the stroma upon vascular challenge: regulation of cytokines and MMPs levels

CD31, vWF and VEGF values from the supernatant showed higher or similar values for the vascularized stroma compared to the mono-culture model (Table 1). These results suggest that, despite a lower nominal concentration of ECs in the vascularized stroma, the fibroblast fraction allowed for a sustained expression of endothelial markers.

As for VEGF expression, BEV induced a drastic decrease of CD31. Analyses conducted on tumor biopsies and *in vivo* experiments upon BEV administration have indeed showed an impaired CD31 expression, most likely correlated to the VEGF drop, suggesting a VEGF-regulated mechanism of CD31 production in ECs. [88,89] Interestingly, CD31 downregulation was also observed under hypoxia, however not accompanied by a higher cytotoxicity, a trend that has been previously correlated to a transition towards a mesenchymal phenotype. [90,91] No significant variations of CD31 levels was observed upon L-Arg administration. The CD31 diminution was mediated in the vascularized stroma model, for which an attenuated reduction was observed. These results suggested that, although both pro and anti-angiogenic cues can induce similar cytokine levels, different pathways are triggered: in one case, the response to hypoxia was related to a sustained cellular viability, while in the case of BEV, loss of morphology, functionality and viability were observed.

Basic fibroblast growth factor (bFGF) has been previously demonstrated to increase in ECs 2D cultures treated with BEV, along with augmented MMP-2 expression. [92] Our data showed the same trend in the vascular model, with bFGF being of 77 pg mL^{-1} upon BEV administration compared to 53 pg mL^{-1} for the control, while an increase in the vascularized stroma model was observed in the first hour upon administration, followed by recovery of basal values (Fig. S12, Appendix). Similarly, bFGF has been shown to be required for ECs angiogenesis under hypoxia, in line with the increase for the hypoxia condition in the monoculture. [93] In our CO-CULT model, constant values of bFGF released were observed, suggesting its role in mediating these complex mechanisms.

An increased production of interleukin-8 (IL-8) for the vascularized stroma in untreated condition was also noticed, coherent with the role played by fibroblasts in the inflammation regulatory pathways. [94,95] External cues did not induce any significant changes in IL-8 concentration, underlying the capability of the stroma to effectively respond to the external stimuli, without triggering an inflammatory response.

Results from the MMPs analyses revealed the differential response

mediated by the fibroblasts, as we observed lower MMP-9 values for the vascularized stroma model compared to the control (Fig. S13a, Appendix). MMP-9 values decreased under treatment for the vascularized stroma and increased in the monoculture upon L-Arg and BEV administration. As the action of NO on MMPs (MMP-9 and MMP-2, particularly) regulation has been previously reported, the results of MMPs expression for the vascular mono-culture model were coherent with the upregulation of nitric oxide levels discussed above. [59] In case of BEV treatment, higher MMPs 9 and 2 have been shown from plasma levels in clinical studies, and potentially considered a predictive markers of BEV treatment efficiency. [96,97] These results thus showed the capability of our model to closely mimic a physiological response to drug administration.

Values of MMP-2 were instead upregulated for the co-culture, being two orders of magnitude higher than for the vascular tissue (Fig. S13b, Appendix). These results suggested an important matrix remodeling operated by the fibroblast fraction and likely correlated to IL-8 values, with a peak for the BEV treatment. [98] Although these values were not comparable with other data found in literature due to use of different *in vitro* models or analysis techniques, the trends suggested a capability of the 3D stroma to functionally react to the cues and actively initiate a matrix remodeling under hypoxia and bevacizumab administration. Moreover, as chemokines production and MMPs release have been identified among the main characters of cancer-associated matrix remodeling, tumor angiogenesis and invasion mechanism, we believe that our 3D model could serve as *in vitro* platform for studies of these pathological conditions and further investigation of related therapeutics. [99–101]

4. Conclusion

In summary, we have designed a 3D vascularized stroma model that exhibited physiological-like response to administered angiogenic cues. The *in vitro* platform aimed to address some of the current limitations in TE, notably the lack of vasculature and the underrepresentation of stroma-mediated response. Here, we proposed a pullulan/dextran-based porous scaffold with tunable physical and mechanical properties. Firstly, the matrix was used to implement a functional vascular lumen and then for integration of the fibroblastic fraction to reproduce human vascularized stroma, by following a dual step co-culturing procedure. Imaging was performed without sectioning by confocal, bi-photon and lightsheet microscopy to preserve the 3D structure and information, upon development of an optical clearing protocol adapted to our biomaterial. The model was subjected to different external cues, namely hypoxic environment, administration of the amino acid L-Arginine and of the anti-VEGF drug bevacizumab, and its response compared to a mono-cultured vascular model. The results underlined the protective and beneficial role of fibroblasts on the vascular fraction, as increased viability, regulation of nitric oxide levels, cytokines and active ECM remodeling.

This work opens new ways for fabricating more complex multicellular models, by integration of other stroma cell types, such as lymphocytes and macrophages, and vascular cell types, as pericytes, and for integrating parenchymal and epithelial cells to mimic specific tissues. Further studies should be envisioned to introduce dynamic perfusion of the constructs and to improve in-depth imaging of the vascular networks. More widely, as stroma is known to play a key role in mediating many pathology-related mechanisms, we believe that this platform can be used for *in vitro* disease modeling for both fundamental and applicative studies, such as drug screening and pharmacodynamics.

Supplementary data to this article can be found online at https://doi.org/10.1016/j.bioadv.2023.213636.

CRediT authorship contribution statement

Alessandra Dellaquila: Conceptualization, Methodology, Validation, Data curation, Formal analysis, Investigation, Project administration, Writing – original draft, Writing – review & editing. **Chloé Dujardin:** Conceptualization, Methodology, Validation, Investigation, Formal analysis, Writing – review & editing. **Chau Le Bao:** Methodology, Investigation. **Chloé Chaumeton:** Methodology, Investigation, Writing – review & editing. **Albane Carré:** Methodology, Investigation, Writing – review & editing. **Camille Le Guilcher:** Methodology, Investigation. **France Lam:** Methodology, Investigation, Resources, Writing – review & editing. **Teresa Simon-Yarza:** Conceptualization, Supervision, Funding acquisition, Resources, Project administration, Writing – review & editing.

Declaration of competing interest

The authors declare no competing financial interests nor personal relationships that could have influenced the work reported here.

Data availability

Data will be made available on request.

Acknowledgements

This project has received funding from the French Research Agency ANR under the project “EXCALYBUR” (Grant No. ANR-20-CE18-0001-01) and from IdEx – Émergence en Recherche, Université de Paris Cité under the project “POLCA”. A.D. was partially financed by the European Union’s Horizon 2020 research and innovation program under the Marie Sklodowska-Curie project “DeLIVER” (Grant Agreement No. 766181). C. D. was funded by the AMX program of the Ecole Polytechnique and the French ministry for Higher Education and Research. The authors gratefully acknowledge the Photonic Imaging Platform IMA’CRI (Centre de recherche sur l’Inflammation- CRI, INSERM) and Dr. Samira Benadda for their support and assistance in this work. The authors would like to acknowledge Dr. Jean-Philippe Desilles for his help in the project and Dr. Didier Letourneur for the constructive discussion.

References

[1] A. Dellaquila, C. Le Bao, D. Letourneur, T. Simon-Yarza, In vitro strategies to vascularize 3D physiologically relevant models, Adv. Sci. 2100798 (2021), https://doi.org/10.1002/ADVS.202100798.
[2] J. Rouwkema, N.C. Rivron, C.A. van Blitterswijk, Vascularization in tissue engineering, Trends Biotechnol. 26 (2008) 434–441, https://doi.org/10.1016/j.tibtech.2008.04.009.
[3] J. Rouwkema, A. Khademhosseini, Vascularization and angiogenesis in tissue engineering: beyond creating static networks, Trends Biotechnol. 34 (2016) 733–745, https://doi.org/10.1016/j.tibtech.2016.03.002.
[4] S. Kim, W. Kim, S. Lim, J.S. Jeon, Vasculature-on-a-chip for in vitro disease models, Bioeng. 4 (2017) 8, https://doi.org/10.3390/BIOENGINEERING4010008.
[5] S. Kim, H. Lee, M. Chung, N.L. Jeon, Engineering of functional, perfusable 3D microvascular networks on a chip, Lab Chip 13 (2013) 1489–1500, https://doi.org/10.1039/c3lc41320a.
[6] D.B. Kolesky, K.A. Homan, M.A. Skylar-Scott, J.A. Lewis, Three-dimensional bioprinting of thick vascularized tissues, Proc. Natl. Acad. Sci. U. S. A. 113 (2016) 3179–3184, https://doi.org/10.1073/pnas.1521342113.
[7] K. Haase, R.D. Kamm, Advances in on-chip vascularization, Regen. Med. 12 (2017) 285–302, https://doi.org/10.2217/rme-2016-0152.
[8] M.G. Kolonin, K.W. Evans, S.A. Mani, R.H. Gomer, Alternative origins of stroma in normal organs and disease, Stem Cell Res. 8 (2012) 312–323, https://doi.org/10.1016/J.SCR.2011.11.005.
[9] E. Colombo, M.G. Cattaneo, Multicellular 3D models to study tumour-stroma interactions, Int. J. Mol. Sci. 22 (2021), https://doi.org/10.3390/ijms22041633.
[10] J. Rodrigues, M.A. Heinrich, L.M. Teixeira, J. Prakash, 3D in vitro model (R) evolution: unveiling tumor–stroma interactions, Trends Cancer 7 (2021) 249–264, https://doi.org/10.1016/j.trecan.2020.10.009.
[11] J.S. Jeon, S. Bersini, M. Gilardi, G. Dubini, J.L. Charest, M. Moretti, R.D. Kamm, Human 3D vascularized organotypic microfluidic assays to study breast cancer cell extravasation, Proc. Natl. Acad. Sci. 112 (2015) 214–219, https://doi.org/10.1073/pnas.1417115112.
[12] H. Kobayashi, T. Shimizu, M. Yamato, K. Tono, H. Masuda, T. Asahara, H. Kasanuki, T. Okano, Fibroblast sheets co-cultured with endothelial progenitor

cells improve cardiac function of infarcted hearts, J. Artif. Organs 11 (2008) 141–147, https://doi.org/10.1007/s10047-008-0421-8.
[13] B. Hendrickx, K. Verdonck, S. Van den Berge, S. Dickens, E. Eriksson, J. J. Vranckx, A. Luttun, Integration of blood outgrowth endothelial cells in dermal fibroblast sheets promotes full thickness wound healing, Stem Cells 28 (2010) 1165–1177, https://doi.org/10.1002/stem.445.
[14] Y. Yao, Z. Dong, Y. Liao, P. Zhang, J. Ma, J. Gao, F. Lu, Adipose extracellular matrix/stromal vascular fraction gel: a novel adipose tissue–derived injectable for stem cell therapy, Plast. Reconstr. Surg. 139 (2017). https://journals.lww.com/plasreconsurg/Fulltext/2017/04000/Adipose_Extracellular_Matrix_Stromal_Vascular.19.aspx.
[15] F. Bersani, J. Lee, M. Yu, R. Morris, R. Desai, S. Ramaswamy, M. Toner, D. A. Haber, B. Parekkadan, Bioengineered implantable scaffolds as a tool to study stromal-derived factors in metastatic cancer models, Cancer Res. 74 (2014) 7229–7238, https://doi.org/10.1158/0008-5472.CAN-14-1809/651636/AM/BIOENGINEERED-IMPLANTABLE-SCAFFOLDS-AS-A-TOOL-TO.
[16] P. Gupta, P.A. Pérez-Mancera, H. Kocher, A. Nisbet, G. Schettino, E.G. Velliou, A novel scaffold-based hybrid multicellular model for pancreatic ductal adenocarcinoma—toward a better mimicry of the in vivo tumor microenvironment, Front. Bioeng. Biotechnol. 8 (2020) 290, https://doi.org/10.3389/FBIOE.2020.00290/BIBTEX.
[17] G. Rijal, W. Li, A versatile 3D tissue matrix scaffold system for tumor modeling and drug screening, Sci. Adv. 3 (2023), e1700764, https://doi.org/10.1126/sciadv.1700764.
[18] C. Le Guilcher, G. Merlen, A. Dellaquila, M.-N. Labour, R. Aid, T. Tordjmann, D. Letourneur, T. Simon-Yarza, Engineered human liver based on pullulan-dextran hydrogel promotes mice survival after liver failure, Mater. Today Bio. 100554 (2023), https://doi.org/10.1016/j.mtbio.2023.100554.
[19] G. Gerschenfeld, R. Aid, T. Simon-Yarza, S. Lanouar, P. Charnay, D. Letourneur, P. Topilko, Tuning physicochemical properties of a macroporous polysaccharide-based scaffold for 3D neuronal culture, Int. J. Mol. Sci. 22 (2021) 12726, https://doi.org/10.3390/IJMS222312726.
[20] C. Le Bao, H. Waller, A. Dellaquila, D. Peters, J. Lakey, F. Chaubet, T. Simon-Yarza, Spatial-controlled coating of pro-angiogenic proteins on 3D porous hydrogels guides endothelial cell behavior, Int. J. Mol. Sci. 23 (2022).
[21] M.-N. Labour, C. Le Guilcher, R. Aid-Launais, N. El Samad, S. Lanouar, T. Simon-Yarza, D. Letourneur, Development of 3D hepatic constructs within polysaccharide-based scaffolds with tunable properties, Int. J. Mol. Sci. Artic. (2020), https://doi.org/10.3390/ijms21103644.
[22] T. Simon-Yarza, M.N. Labour, R. Aid, D. Letourneur, Channeled polysaccharide-based hydrogel reveals influence of curvature to guide endothelial cell arrangement in vessel-like structures, Mater. Sci. Eng. C 118 (2021) 111369, https://doi.org/10.1016/j.msec.2020.111369.
[23] A. Autissier, C. Le Visage, C. Pouzet, F. Chaubet, D. Letourneur, Fabrication of porous polysaccharide-based scaffolds using a combined freeze-drying/cross-linking process, Acta Biomater. 6 (2010) 3640–3648, https://doi.org/10.1016/j.actbio.2010.03.004.
[24] C. Le Visage, D. Letourneur, F. Chaubet, A. Autissier, US9522218B2. https://patents.google.com/patent/US9522218B2/en, 2017 (accessed May 31, 2021).
[25] N. Gostynska, G.S. Krishnakumar, E. Campodoni, S. Panseri, M. Montesi, S. Sprio, E. Kon, M. Marcacci, A. Tampieri, M. Sandri, 3D porous collagen scaffolds reinforced by glycation with ribose for tissue engineering application, Biomed. Mater. 12 (2017), 055002, https://doi.org/10.1088/1748-605X/AA7694.
[27] H. Mollica, Y.J. Teo, A.S.M. Tan, D.Z.M. Tan, P. Decuzzi, A. Pavesi, G. Adriani, A 3D pancreatic tumor model to study T cell infiltration, Biomater. Sci. 9 (2021) 7420–7431.
[28] W. Masselink, D. Reumann, P. Murawala, P. Pasierbek, Y. Taniguchi, F. Bonnay, K. Meixner, J.A. Knoblich, E.M. Tanaka, Broad applicability of a streamlined ethyl cinnamate-based clearing procedure, Dev. 146 (2019), dev166884, https://doi.org/10.1242/DEV.166884/VIDEO-3.
[29] L. Chen, G. Li, Y. Li, Y. Li, H. Zhu, L. Tang, P. French, J. McGinty, S. Ruan, UbasM: an effective balanced optical clearing method for intact biomedical imaging, Sci. Rep. 7 (2017) 12218, https://doi.org/10.1038/s41598-017-12484-3.
[30] J. Schindelin, I. Arganda-Carreras, E. Frise, V. Kaynig, M. Longair, T. Pietzsch, S. Preibisch, C. Rueden, S. Saalfeld, B. Schmid, J.Y. Tinevez, D.J. White, V. Hartenstein, K. Eliceiri, P. Tomancak, A. Cardona, Fiji: an open-source platform for biological-image analysis, Nat. Methods 9 (2012) 676–682, https://doi.org/10.1038/nmeth.2019.
[31] R.S. Singh, N. Kaur, V. Rana, J.F. Kennedy, Recent insights on applications of pullulan in tissue engineering, Carbohydr. Polym. 153 (2016) 455–462, https://doi.org/10.1016/j.carbpol.2016.07.118.
[32] G. Sun, J.J. Mao, Engineering dextran-based scaffolds for drug delivery and tissue repair, Nanomedicine 7 (2012) 1771–1784, https://doi.org/10.2217/nnm.12.149.
[33] A. Hasan, A. Paul, N.E. Vrana, X. Zhao, A. Memic, Y.S. Hwang, M.R. Dokmeci, A. Khademhosseini, Microfluidic techniques for development of 3D vascularized tissue, Biomaterials 35 (2014) 7308–7325, https://doi.org/10.1016/j.biomaterials.2014.04.091.
[34] J. Tien, Microfluidic approaches for engineering vasculature, Curr. Opin. Chem. Eng. 3 (2014) 36–41, https://doi.org/10.1016/j.coche.2013.10.006.
[35] J. Tien, Y.W. Dance, Microfluidic Biomaterials, Adv. Healthc. Mater. 10 (2021) 2001028, https://doi.org/10.1002/adhm.202001028.
[36] M.-N. Labour, C. Le Guilcher, R. Aid-Launais, N. El Samad, S. Lanouar, T. Simon-Yarza, D. Letourneur, Development of 3D hepatic constructs within polysaccharide-based scaffolds with tunable properties, Int. J. Mol. Sci. 21 (2020) 3644, https://doi.org/10.3390/ijms21103644.
[37] V.W. Wong, K.C. Rustad, M.G. Galvez, E. Neofytou, J.P. Glotzbach, M. Januszyk, M.R. Major, M. Sorkin, M.T. Longaker, J. Rajadas, G.C. Gurtner, Engineered pullulan–collagen composite dermal hydrogels improve early cutaneous wound healing, Tissue Eng. Part A 17 (2010) 631–644, https://doi.org/10.1089/ten.tea.2010.0298.
[38] X. Li, W. Xue, Y. Liu, W. Li, D. Fan, C. Zhu, Y. Wang, HLC/pullulan and pullulan hydrogels: their microstructure, engineering process and biocompatibility, Mater. Sci. Eng. C 58 (2016) 1046–1057, https://doi.org/10.1016/j.msec.2015.09.039.
[39] D. Atila, D. Keskin, A. Tezcaner, Crosslinked pullulan/cellulose acetate fibrous scaffolds for bone tissue engineering, Mater. Sci. Eng. C 69 (2016) 1103–1115, https://doi.org/10.1016/j.msec.2016.08.015.
[40] J. Wei, J. Yao, M. Yan, Y. Xie, P. Liu, Y. Mao, X. Li, The role of matrix stiffness in cancer stromal cell fate and targeting therapeutic strategies, Acta Biomater. 150 (2022) 34–47, https://doi.org/10.1016/j.actbio.2022.08.005.
[41] C.F. Guimarães, L. Gasperini, A.P. Marques, R.L. Reis, The stiffness of living tissues and its implications for tissue engineering, Nat. Rev. Mater. 5 (2020) 351–370, https://doi.org/10.1038/s41578-019-0169-1.
[42] N.V. Goncharov, A.D. Nadeev, R.O. Jenkins, P.V. Avdonin, Markers and biomarkers of endothelium: when something is rotten in the state, Oxid. Med. Cell. Longev. 2017 (2017).
[43] A. Dellaquila, Doctoral Thesis, Universität Bielefeld, 2021.
[44] M.L. Iruela-Arispe, C.A. Diglio, E.H. Sage, Modulation of extracellular matrix proteins by endothelial cells undergoing angiogenesis in vitro, Arterioscler. Thromb. J. Vasc. Biol. 11 (1991) 805–815, https://doi.org/10.1161/01.ATV.11.4.805.
[45] G. Kundrotas, Surface markers distinguishing mesenchymal stem cells from fibroblasts, Acta Medica Litu. 19 (2012) 75–79.
[46] D. Jiang, Y. Rinkevich, Defining skin fibroblastic cell types beyond CD90, Front. Cell Dev. Biol. 6 (2018), https://doi.org/10.3389/fcell.2018.00133.
[47] A. Bhattacharjee, D.S. Katti, Pore alignment in gelatin scaffolds enhances chondrogenic differentiation of infrapatellar fat pad derived mesenchymal stromal cells, ACS Biomater Sci. Eng. 5 (2019) 114–125, https://doi.org/10.1021/acsbiomaterials.8b00246.
[48] S.R. Caliari, B.A.C. Harley, The effect of anisotropic collagen-GAG scaffolds and growth factor supplementation on tendon cell recruitment, alignment, and metabolic activity, Biomaterials 32 (2011) 5330–5340.
[49] J. Kobayashi, A. Kikuchi, T. Aoyagi, T. Okano, Cell sheet tissue engineering: cell sheet preparation, harvesting/manipulation, and transplantation, J. Biomed. Mater. Res. Part A. 107 (2019) 955–967, https://doi.org/10.1002/jbm.a.36627.
[50] M. Cantini, H. Donnelly, M.J. Dalby, M. Salmeron-Sanchez, The plot thickens: the emerging role of matrix viscosity in cell mechanotransduction, Adv. Healthc. Mater. 9 (2020) 1901259, https://doi.org/10.1002/adhm.201901259.
[51] Y. Chau, Y. Luo, A.C.Y. Cheung, Y. Nagai, S. Zhang, J.B. Kobler, S.M. Zeitels, R. Langer, Incorporation of a matrix metalloproteinase-sensitive substrate into self-assembling peptides – a model for biofunctional scaffolds, Biomaterials 29 (2008) 1713–1719, https://doi.org/10.1016/j.biomaterials.2007.11.046.
[52] E.A. Calle, S. Vesuna, S. Dimitrievska, K. Zhou, A. Huang, L. Zhao, L.E. Niklason, M.J. Levene, The use of optical clearing and multiphoton microscopy for investigation of three-dimensional tissue-engineered constructs, Tissue Eng. Part C Methods 20 (2013) 570–577, https://doi.org/10.1089/ten.tec.2013.0538.
[53] A.A. Appel, M.A. Anastasio, J.C. Larson, E.M. Brey, Imaging challenges in biomaterials and tissue engineering, Biomaterials 34 (2013) 6615–6630, https://doi.org/10.1016/j.biomaterials.2013.05.033.
[54] R.E. Guldberg, C.L. Duvall, A. Peister, M.E. Oest, A.S.P. Lin, A.W. Palmer, M. E. Levenston, 3D imaging of tissue integration with porous biomaterials, Biomaterials 29 (2008) 3757–3761, https://doi.org/10.1016/j.biomaterials.2008.06.018.
[55] S. Tseng, Y.-H. Lee, Z.-H. Chen, H.-H. Lin, C.-Y. Lin, S.-C. Tang, Integration of optical clearing and optical sectioning microscopy for three-dimensional imaging of natural biomaterial scaffolds in thin sections, J. Biomed. Opt. 14 (2009) 44004, https://doi.org/10.1117/1.3158998.
[56] R.D. Hume, S. Pensa, E.J. Brown, P.A. Kreuzaler, J. Hitchcock, A. Husmann, J. J. Campbell, A.O. Lloyd-Thomas, R.E. Cameron, C.J. Watson, Tumour cell invasiveness and response to chemotherapeutics in adipocyte invested 3D engineered anisotropic collagen scaffolds, Sci. Rep. 8 (2018) 12658, https://doi.org/10.1038/s41598-018-30107-3.
[57] D.S. Richardson, J.W. Lichtman, Clarifying tissue clearing, Cell 162 (2015) 246–257, https://doi.org/10.1016/J.CELL.2015.06.067.
[58] T. Yu, J. Zhu, D. Li, D. Zhu, Physical and chemical mechanisms of tissue optical clearing, IScience 24 (2021) 102178, https://doi.org/10.1016/j.isci.2021.102178.
[59] M. Jahani, M. Azadbakht, H. Rasouli, R. Yarani, D. Rezazadeh, N. Salari, K. Mansouri, L-arginine/5-fluorouracil combination treatment approaches cells selectively: rescuing endothelial cells while killing MDA-MB-468 breast cancer cells, Food Chem. Toxicol. 123 (2019) 399–411, https://doi.org/10.1016/j.fct.2018.11.018.
[60] J. Veldhuizen, R. Chavan, B. Moghadas, J.G. Park, V.D. Kodibagkar, R.Q. Migrino, M. Nikkhah, Cardiac ischemia on-a-chip to investigate cellular and molecular response of myocardial tissue under hypoxia, Biomaterials 281 (2022) 121336, https://doi.org/10.1016/j.biomaterials.2021.121336.
[61] S.H. Kim, J.W. Kim, Comparison of the effects between bevacizumab and mitomycin C on the survival of fibroblasts, J. Korean Ophthalmol. Soc. 52 (2011) 345–349, https://doi.org/10.3341/JKOS.2011.52.3.345.
[62] M.Á. Olmedo-Suárez, T. Sekiguchi, A. Takano, M.D. Cañizares-Macías, N. Futai, Integrated on-chip 3D vascular network culture under hypoxia, Micromachines 11 (2020), https://doi.org/10.3390/mi11050475.

[63] C. Liverani, A. De Vita, S. Minardi, Y. Kang, L. Mercatali, D. Amadori, A. Bongiovanni, F. La Manna, T. Ibrahim, E. Tasciotti, A biomimetic 3D model of hypoxia-driven cancer progression, Sci. Rep. 9 (2019) 12263, https://doi.org/10.1038/s41598-019-48701-4.
[64] M. Ziche, L. Morbidelli, Nitric oxide and angiogenesis, J. Neurooncol 50 (2000) 139–148, https://doi.org/10.1023/A:1006431309841.
[65] H. Kimura, H. Esumi, Reciprocal regulation between nitric oxide and vascular endothelial growth factor in angiogenesis, Acta Biochim. Pol. 50 (2003) 49–59.
[66] Y. Yu, J. Chen, R. Chen, L. Cao, W. Tang, D. Lin, J. Wang, C. Liu, Enhancement of VEGF-mediated angiogenesis by 2-N,6-O-sulfated chitosan-coated hierarchical PLGA scaffolds, ACS Appl. Mater. Interfaces 7 (2015) 9982–9990, https://doi.org/10.1021/acsami.5b02324.
[67] N.W. Rajapakse, D.L. Mattson, Role of L-arginine in nitric oxide production in health and hypertension, Clin. Exp. Pharmacol. Physiol. 36 (2009) 249–255, https://doi.org/10.1111/j.1440-1681.2008.05123.x.
[68] R.H. Böger, The pharmacodynamics of L-arginine, J. Nutr. 137 (2007) 1650S–1655S, https://doi.org/10.1093/jn/137.6.1650S.
[69] R.H. Böger, S.M. Bode-Böger, The clinical pharmacology of L-arginine, Annu. Rev. Pharmacol. Toxicol. 41 (2001) 79–99, https://doi.org/10.1146/annurev.pharmtox.41.1.79.
[70] N. Ferrara, K.J. Hillan, H.-P. Gerber, W. Novotny, Discovery and development of bevacizumab, an anti-VEGF antibody for treating cancer, Nat. Rev. Drug Discov. 3 (2004) 391–400, https://doi.org/10.1038/nrd1381.
[71] J. Garcia, H.I. Hurwitz, A.B. Sandler, D. Miles, R.L. Coleman, R. Deurloo, O. L. Chinot, Bevacizumab (Avastin®) in cancer treatment: a review of 15 years of clinical experience and future outlook, Cancer Treat. Rev. 86 (2020) 102017, https://doi.org/10.1016/j.ctrv.2020.102017.
[72] C. Kim, J. Kasuya, J. Jeon, S. Chung, R.D. Kamm, A quantitative microfluidic angiogenesis screen for studying anti-angiogenic therapeutic drugs, Lab Chip 15 (2015) 301–310.
[73] D.J. Manalo, A. Rowan, T. Lavoie, L. Natarajan, B.D. Kelly, S.Q. Ye, J.G.N. Garcia, G.L. Semenza, Transcriptional regulation of vascular endothelial cell responses to hypoxia by HIF-1, Blood 105 (2005) 659–669, https://doi.org/10.1182/blood-2004-07-2958.
[74] M.E. Hubbi, G.L. Semenza, Regulation of cell proliferation by hypoxia-inducible factors, Am. J. Physiol. Physiol. 309 (2015) C775–C782, https://doi.org/10.1152/ajpcell.00279.2015.
[75] J.M. Bosmans, C.J. Vrints, M.M. Kockx, H. Bult, K.M.C. Cromheeke, A.G. Herman, Continuous perivascular l-arginine delivery increases total vessel area and reduces neointimal thickening after experimental balloon dilatation, Arterioscler. Thromb. Vasc. Biol. 19 (1999) 767–776, https://doi.org/10.1161/01.ATV.19.3.767.
[76] J. Kolenda, S.S. Jensen, C. Aaberg-Jessen, K. Christensen, C. Andersen, N. Brünner, B.W. Kristensen, Effects of hypoxia on expression of a panel of stem cell and chemoresistance markers in glioblastoma-derived spheroids, J. Neurooncol 103 (2011) 43–58, https://doi.org/10.1007/s11060-010-0357-8.
[77] Y. Sun, C. Jiang, H. Hong, J. Liu, L. Qiu, Y. Huang, L. Ye, Effects of hypoxia on cardiomyocyte proliferation and association with stage of development, Biomed. Pharmacother. 118 (2019) 109391, https://doi.org/10.1016/j.biopha.2019.109391.
[78] H. Yang, M.J. Jager, H.E. Grossniklaus, Bevacizumab suppression of establishment of micrometastases in experimental ocular melanoma, Invest. Ophthalmol. Vis. Sci. 51 (2010) 2835–2842, https://doi.org/10.1167/iovs.09-4755.
[79] Ö. Moraloglu, H. Işık, S. Kılıç, U. Şahin, M. Çaydere, H. Üstün, S. Batıoglu, Effect of bevacizumab on postoperative adhesion formation in a rat uterine horn adhesion model and the correlation with vascular endothelial growth factor and Ki-67 immunopositivity, Fertil. Steril. 95 (2011) 2638–2641, https://doi.org/10.1016/j.fertnstert.2011.02.005.
[80] C.-L. Chen, C.-M. Liang, Y.-H. Chen, M.-C. Tai, D.-W. Lu, J.-T. Chen, Bevacizumab modulates epithelial-to-mesenchymal transition in the retinal pigment epithelial cells via connective tissue growth factor up-regulation, Acta Ophthalmol. 90 (2012) e389–e398, https://doi.org/10.1111/j.1755-3768.2012.02426.x.
[81] C.V. Suschek, O. Schnorr, K. Hemmrich, O. Aust, L.-O. Klotz, H. Sies, V. Kolb-Bachofen, Critical role of l-arginine in endothelial cell survival during oxidative stress, Circulation 107 (2003) 2607–2614, https://doi.org/10.1161/01.CIR.0000066909.13953.F1.
[82] E. Dinc, O. Yildirim, L. Ayaz, T. Ozcan, S.N. Yilmaz, Effects of intravitreal injection of bevacizumab on nitric oxide levels, Eye 29 (3) (2015) 436–442, https://doi.org/10.1038/eye.2014.297.
[83] S.H. Kim, J.W. Kim, Effect of bevacizumab on survival and production of nitric oxide in trabecular meshwork cells, J. Korean Ophthalmol. Soc. 50 (2009) 1404–1408, https://doi.org/10.3341/JKOS.2009.50.9.1404.
[84] J.W. Song, D. Bazou, L.L. Munn, Anastomosis of endothelial sprouts forms new vessels in a tissue analogue of angiogenesis, Integr. Biol. 4 (2012) 857–862, https://doi.org/10.1039/c2ib20061a.
[85] H. Lee, W. Park, H. Ryu, N.L. Jeon, A microfluidic platform for quantitative analysis of cancer angiogenesis and intravasation, Biomicrofluidics. 8 (2014) 54102.
[86] C. Lin, D. Malik, J. Cáceres-del-Carpio, M. Tarek, R.D. Costa, D.S. Boyer, C. M. Kenney, B. Kuppermann, Reactive oxygen species levels in human retinal pigment epithelium cells in vitro to anti-VEGF agents: ranibizumab, bevacizumab, aflibercept and Ziv-aflibercept, Invest. Ophthalmol. Vis. Sci. 56 (2015) 1518.
[87] J. Tejero, S. Shiva, M.T. Gladwin, Sources of vascular nitric oxide and reactive oxygen species and their regulation, Physiol. Rev. 99 (2018) 311–379, https://doi.org/10.1152/physrev.00036.2017.
[88] S.X. Yang, S.M. Steinberg, D. Nguyen, T.D. Wu, Z. Modrusan, S.M. Swain, Gene expression profile and Angiogenic markers correlate with response to neoadjuvant bevacizumab followed by bevacizumab plus chemotherapy in breast cancer, Clin. Cancer Res. 14 (2008) 5893–5899, https://doi.org/10.1158/1078-0432.CCR-07-4762.
[89] H. Yang, M.J. Jager, H.E. Grossniklaus, Bevacizumab suppression of establishment of micrometastases in experimental ocular melanoma, Invest. Ophthalmol. Vis. Sci. 51 (2010) 2835–2842, https://doi.org/10.1167/IOVS.09-4755.
[90] G. Musumeci, A. Castorina, G. Magro, V. Cardile, S. Castorina, D. Ribatti, Enhanced expression of CD31/platelet endothelial cell adhesion molecule 1 (PECAM1) correlates with hypoxia inducible factor-1 alpha (HIF-1α) in human glioblastoma multiforme, Exp. Cell Res. 339 (2015) 407–416, https://doi.org/10.1016/j.yexcr.2015.09.007.
[91] B. Zhang, W. Niu, H. Dong, M. Liu, Y. Luo, Z. Li, Hypoxia induces endothelial-mesenchymal transition in pulmonary vascular remodeling, Int. J. Mol. Med. 42 (2018) 270–278, https://doi.org/10.3892/ijmm.2018.3584.
[92] M. Zhang, S. Chu, F. Zeng, H. Xu, Bevacizumab modulates the process of fibrosis in vitro, Clin. Exp. Ophthalmol. 43 (2015) 173–179, https://doi.org/10.1111/ceo.12374.
[93] M. Calvani, A. Rapisarda, B. Uranchimeg, R.H. Shoemaker, G. Melillo, Hypoxic induction of an HIF-1alpha-dependent bFGF autocrine loop drives angiogenesis in human endothelial cells, Blood 107 (2006) 2705–2712, https://doi.org/10.1182/blood-2005-09-3541.
[94] B.S. Qazi, K. Tang, A. Qazi, Recent advances in underlying pathologies provide insight into interleukin-8 expression-mediated inflammation and angiogenesis, Int. J. Inflam. 2011 (2011) 908468, https://doi.org/10.4061/2011/908468.
[95] C.G. Larsen, A.O. Anderson, J.J. Oppenheim, K. Matsushima, Production of interleukin-8 by human dermal fibroblasts and keratinocytes in response to interleukin-1 or tumour necrosis factor, Immunology 68 (1989) 31–36.
[96] O.L. Chinot, J. Garcia, S. Romain, C. Revil, T. Cloughesy, W.P. Mason, R. Nishikawa, R. Henriksson, F. Saran, A.F. Carpentier, Baseline plasma matrix metalloproteinase 9 (MMP9) to predict overall survival (OS) benefit from bevacizumab (BEV) in newly diagnosed glioblastoma (GBM): Retrospective analysis of AVAglio, 2016.
[97] E. Tabouret, A. Goncalves, F. Bertucci, J.-Y. Pierga, T. Petit, C. Levy, J.-M. Ferrero, M. Campone, J. Gligorov, F. Lerebours, Effect of high MMP2 and low MMP9 baseline serum levels on outcome in patients with HER2-positive inflammatory breast cancer (IBC) treated with bevacizumab (BEV)-and trastuzumab (TRA)-based neoadjuvant chemotherapy (NAC) in the BEVERLY 2 study, 2015.
[98] M. Bar-Eli, Role of Interleukin-8 in tumor growth and metastasis of human melanoma, Pathobiology 67 (1999) 12–18, https://doi.org/10.1159/000028045.
[99] M. Xue, K. McKelvey, K. Shen, N. Minhas, L. March, S.-Y. Park, C.J. Jackson, Endogenous MMP-9 and not MMP-2 promotes rheumatoid synovial fibroblast survival, inflammation and cartilage degradation, Rheumatology. 53 (2014) 2270–2279, https://doi.org/10.1093/rheumatology/keu254.
[100] R.S. Boyd, F.R. Balkwill, MMP-2 release and activation in ovarian carcinoma: the role of fibroblasts, Br. J. Cancer 80 (1999) 315–321, https://doi.org/10.1038/sj.bjc.6690357.
[101] K. Kessenbrock, V. Plaks, Z. Werb, Matrix metalloproteinases: regulators of the tumor microenvironment, Cell 141 (2010) 52–67, https://doi.org/10.1016/J.CELL.2010.03.015.